FRACTURE TRANSPORT OF URANIUM AT THE NOPAL I NATURAL ANALOG SITE

Prepared for

Nuclear Regulatory Commission
Contract NRC-02-93-005

Prepared by

Center for Nuclear Waste Regulatory Analyses
San Antonio, Texas

May 1994

CNWRA 94-011

FRACTURE TRANSPORT OF URANIUM AT THE NOPAL I NATURAL ANALOG SITE

Prepared for

Nuclear Regulatory Commission
Contract NRC-02-93-005

Prepared by

English C. Pearcy

Center for Nuclear Waste Regulatory Analyses
San Antonio, Texas

May 1994

PREVIOUS REPORTS IN SERIES

Number	Name	Date Issued
CNWRA 93-012	Uranium Mineralogy of the Nopal I Natural Analog Site, Chihuahua, Mexico	June 1993

ABSTRACT

At the Nopal I uranium (U) deposit, in the Peña Blanca District, Chihuahua, Mexico, U has been transported under conditions comparable to those that could occur at the candidate U.S. high-level waste (HLW) repository at Yucca Mountain, Nevada. This investigation focused on approximately 1,400 m^2 of essentially continuous bedrock outcrop spanning the Nopal I deposit and surrounding host tuff. Data collected document: (i) the distributions of U within and around the Nopal I deposit, (ii) the distribution and characteristics of the fracture network within and surrounding the deposit, and (iii) the transport of U away from the deposit mainly along fracture paths. U-series isotopic measurements indicate mobilization of U along the margin of the deposit within the last 1 Ma and significant U transport at about 54 Ka.

Greater transport distances were achieved along a few relatively continuous mesofractures (i.e., fractures with apertures > 1 mm and traces extending more than 10 m) than through the general fracture network composed of thousands of less continuous microfractures (i.e., fractures with apertures $<< 1$ mm and traces on the order of cm) within and surrounding the deposit. U transport away from the deposit appears to be largely independent of variations in the general fracture network pattern; this interpretation is supported by fractal analyses of the patterns suggesting that this result is insensitive to the scale at which the observations were made. Transport of U away from the Nopal I deposit along effective horizontal mesofracture paths achieved maximum distances at least 20 times greater than transport of U through tuff with a complex network of microfractures. Transport of U away from individual microfractures into homogeneous, unfractured (at optical microscopy scales) tuff matrix appears limited to distances less than 1 mm.

U retardation and retention within a complex microfracture network are 5 times greater than U retardation and retention within a mesofracture through which U was introduced into the microfracture network. Data from individual microfractures with high U concentrations (e.g., 5.6×10^5 ppm) indicate that the amount of U transported out of a microfracture into the tuff matrix adjacent to a microfracture is only 5 percent of the U retained within a microfracture (mainly by precipitation as uranophane). This analysis suggests a relative ranking for U retention: (i) microfracture network retention $>>$ mesofracture retention, and (ii) individual microfracture retention $>>$ matrix retention.

CONTENTS

FIGURES

FIGURES (cont'd)

FIGURES (cont'd)

FIGURES (cont'd)

TABLES

ACKNOWLEDGMENTS

This report was prepared to document work performed by the Center for Nuclear Waste Regulatory Analyses (CNWRA) for the Nuclear Regulatory Commission (NRC) under Contract No. NRC-02-93-005. The activities reported here were performed on behalf of the NRC Office of Nuclear Regulatory Research, Division of Regulatory Applications. The report is an independent product of the CNWRA and does not necessarily reflect the views or regulatory position of the NRC.

Original mapping for this study was largely carried out by Ignacio Reyes of the *Universidad Autonoma de Chihuahua*. Computer programming was provided by Sandy Nguyen, Joseph Bangs, and Edward Harloe. Bret Leslie and James Prikryl supported both field sampling and laboratory analyses. Amitava Ghosh helped with the fractal analysis computations. The SwRI Publications Unit provided editorial, artistic, and production assistance. Comments by William Murphy and H. Lawrence McKague substantially improved this document.

QUALITY OF DATA, ANALYSES AND CODE DEVELOPMENT

DATA: CNWRA-generated laboratory and field data contained in this report meet quality assurance requirements described in the CNWRA Quality Assurance Manual.

ANALYSES AND CODES: Scientific/engineering computer codes used in analyses contained in this report are: ARC/INFO, STEREO, JADE/MDI, ALPHAMAT, and MAESTRO II. These are standard commercially available packages.

1 INTRODUCTION

One of the chief concerns in seeking to establish a geologic repository for high-level nuclear waste (HLW) is the possibility that hazardous radionuclides could escape engineered barriers and be transported to the accessible environment. Movement along fractures in the host rock of a repository is one mechanism by which hazardous radionuclides can be transported to the accessible environment. Nuclear Regulatory Commission (NRC) Iterative Performance Assessment (IPA) indicates that matrix transport is insignificant; all release is associated with fracture flow, and retardation associated with fracture flow is identified by IPA as a critical issue (Wescott et al., 1994). The possibility of fracture transport must be evaluated for the long time periods required for HLW isolation [e.g., 10^4 yr and greater, U.S. Environmental Protection Agency (EPA), 1989]. One approach to this problem is to study fracture transport in natural systems that are analogous to the repository system and that have operated for long time periods.

The Center for Nuclear Waste Regulatory Analyses (CNWRA) has undertaken natural analog research in support of the NRC. The U.S. Nuclear Waste Policy Act of 1982 (NWPA), as amended in 1987, designated Yucca Mountain, Nevada, as the sole candidate site to be characterized for possible permanent disposal of HLW in the United States. The Nopal I U deposit, in the Peña Blanca District, Chihuahua, Mexico, has been identified as analogous in many important aspects to Yucca Mountain (Ildefonse et al., 1990c; Murphy and Pearcy, 1992; Murphy et al., 1991; Pearcy and Murphy, 1991, 1992). Both Yucca Mountain and the Nopal I deposit are located in semi-arid to arid climatic regions (Figure 1-1). The Nopal I deposit is part of a Basin and Range horst composed of Tertiary rhyolitic tuffs underlain by carbonate sedimentary rocks as is Yucca Mountain. Further, both the proposed Yucca Mountain repository horizon and the Nopal I deposit are located in the oxidizing, hydrologically unsaturated zone 100 m or more above the water table (Pearcy et al., 1993a). Material characteristics of uraninite at Nopal I and the spent nuclear fuel proposed for a HLW repository are also generally similar, and mineral alteration assemblages and sequences are comparable (Pearcy et al., 1993b). Earlier work characterizing the Nopal I deposit includes Calas (1977), Cardenas-Flores (1985), George-Aniel et al. (1985), Goodell (1981), Ildefonse et al. (1990a), Leroy et al. (1987), and Muller et al. (1990).

The Nopal I deposit (defined as the volume of rock at Nopal I containing easily visible U mineralization) is roughly cylindrical in form with gross horizontal dimensions of about 18 m by 30 m with a nominal ore zone extending some 100 m vertically. The upper portion of this well-defined body of U mineralization is hosted by heavily fractured, silicic tuffs (Nopal and Coloradas Formations), whereas the lowermost portion of the deposit occurs in a basal conglomerate (Pozos Formation). Mining during the late 1970s and early 1980s exposed the upper portion of the deposit on two broad horizontal surfaces with about 10-m vertical separation (Levels +00 and +10). Together, these surfaces completely span the outcrop of the deposit and expose much of the surrounding host rock, providing an opportunity to study transport of U from the deposit out into the host tuff.

The general objective of this study was to evaluate the Nopal I deposit for evidence of fracture transport of U away from the deposit. Specific objectives of this study were: (i) to determine the distribution of U within and around the deposit; (ii) to map the locations, orientations, and forms of fractures within and around the deposit; (iii) to measure the concentrations of U within fractures that intersect the deposit and in generally fractured rock adjacent to the deposit; and (iv) to measure the concentrations of U transported into the tuff matrix perpendicular to fractures.

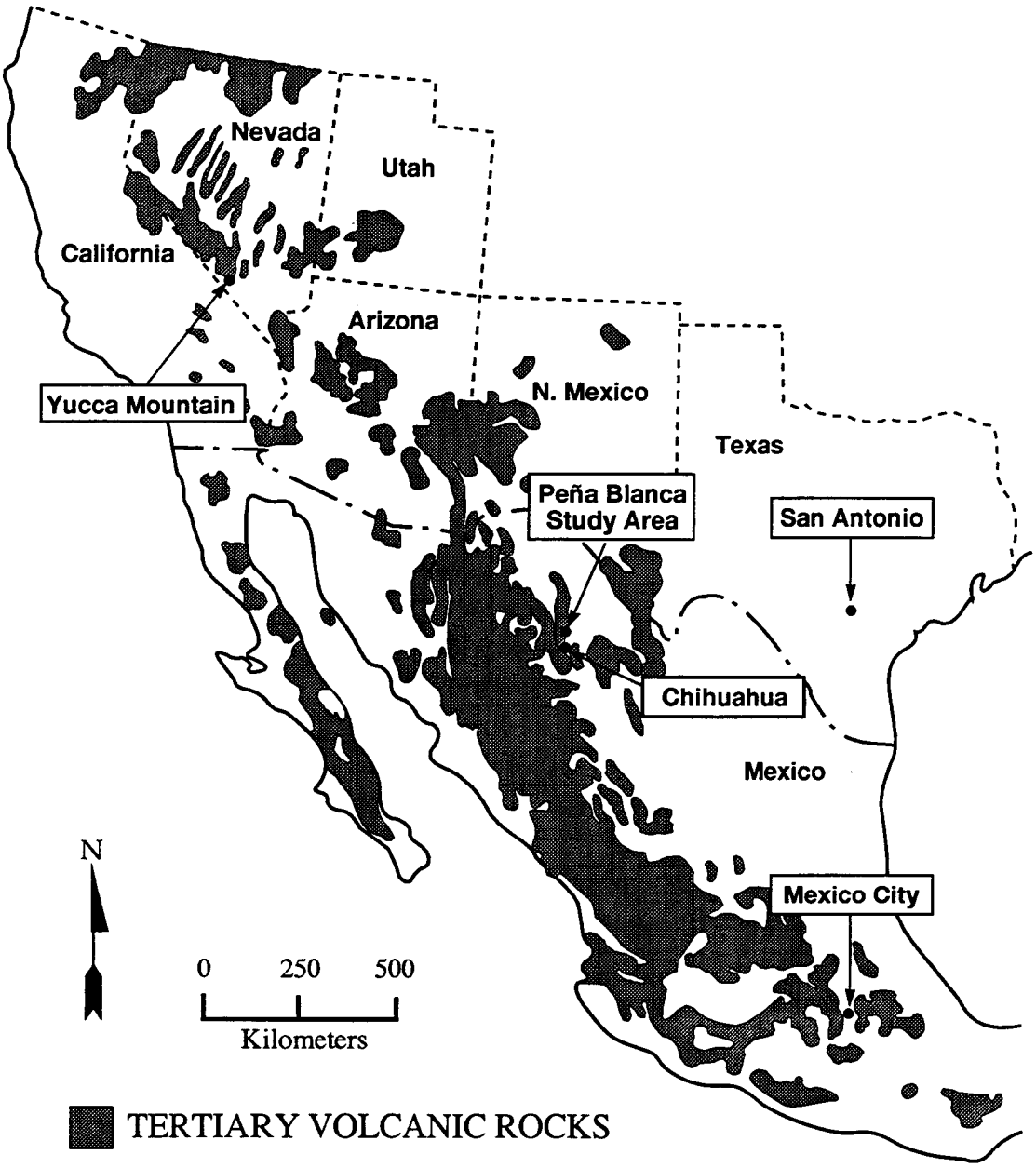

Figure 1-1. The Nopal I U deposit is located in the Peña Blanca mining district, Chihuahua, Mexico. Yucca Mountain, Nevada, the proposed site for the U.S. HLW repository, is located northwest of the Peña Blanca District along a general trend of Tertiary volcanic rocks in the Basin and Range province.

2 METHODS

Portions of Levels +10 and +00 of the Nopal I deposit were cleared of loose rock, soil, and debris; clearing began with picks and shovels and was completed with brooms. This effort provided a nearly continuous bedrock exposure across the outcrop of the deposit and the surrounding tuff (about 1,200 m^2 of the Level +10 surface and about 200 m^2 of Level +00). Spatial control was established using traditional plane table surveying techniques. A permanent 1 m by 1 m grid with axes oriented NS and EW was constructed over the cleared areas using 6.4-cm P-K nails driven into the tuff to provide a location reference framework. This grid provides the location references in this report.

General U distributions within and around the deposit were mapped by gamma intensity. A contact gamma survey of the cleared bedrock areas was conducted with measurements taken at the intersections of the 1 m by 1 m grid lines. Readings (mR/hr) were recorded on a survey meter (Ludlum model 3) equipped with a Geiger-Müller detector (Ludlum model 44-6).

Geologic features of the cleared areas of Levels +10 and +00 were mapped at the detailed scale of 1:25. Occurrence of U minerals, host rock type, and host rock alteration, as well as fracture locations and forms were mapped with reference to the 1 m grid. Fracture orientations were measured using standard Brunton transit techniques. Original field data were drafted on mylar sheets from which they were digitized and compiled with ARC/INFO software for analysis and calculations. Analysis of fracture orientation data was accomplished using STEREO software.

A 28-m length of a major EW fracture set located about 13.5 m N on the reference grid was sampled by collecting portions of fracture-filling minerals at approximately 1-m intervals. The 13.5 m N fracture set is a subplanar feature with a near-vertical dip; the trace of the set is approximately perpendicular to the W margin of the deposit. This fracture set was observed to be the longest and most continuous to intersect the deposit; fracture aperture varies from 2 to 7 mm. Sampling of the material filling the fracture was accomplished by scraping fracture-filling material from the rock surfaces using a steel pocket knife. Five sets of tuff samples were collected perpendicular to the major EW fracture at distances 0.5, 6.0, 10.2, 15.9, and 20.1 m from the edge of the deposit. These locations were chosen as those where traverses could extend from the major EW fracture without crossing or closely approaching another large fracture. These traverse samples were collected by chiseling out small (2- to 5-cm maximum dimension) pieces of tuff.

A 2-m profile across the western margin of the deposit at 9.1 m N was sampled at 20-cm intervals along a path perpendicular to the margin of the deposit at a location chosen to avoid major fractures. The profile area contains abundant small fractures and is thought to be representative of the degree of fracturing of the host rock surrounding the deposit. Bulk tuff samples of 1 to 2 kg were extracted with hammer and chisel.

Samples of the 13.5-m N fracture-filling materials and the tuff from the 9.1-m N transect were powdered and analyzed by x-ray diffractometry (XRD) to determine mineralogy [Automated (RADIX) Siemens D500 XRD; Cu tube, Ni filter, 40 kV, 37 mA; scan 2–70° at 0.02° step; count 1.0 s]. Diffraction patterns were collected electronically with a DATABOX, and the graphics interface program JADE/MDI was used to provide output of the absolute intensity of the diffraction signal at each 0.02° 2-theta angle.

U contents of fracture-filling minerals and bulk rock samples were measured by gamma spectrometry using a Canberra system consisting of an intrinsic germanium detector (30-percent efficiency at 1.33 MeV for ^{60}Co), model 4610 multichannel analyzer board, and system 100 software for data acquisition and analysis. $^{234}U/^{238}U$ ratios were measured by alpha spectrometry with an EG&G ORTEC system including model 576A dual spectrometers with ion-implanted-silicon charged particle detectors, model 920-16 multichannel buffer, ALPHAMAT analysis software for acquisition control, and MAESTRO II multichannel analyzer emulation software for analysis of spectral data.

Autoradiographic analyses were performed on samples from the Nopal site to measure the spatial variation in U concentration perpendicular to microfractures (apertures $<<1$ mm and lengths on the order of cm). This small scale allows observation of U concentrations in portions of the tuff matrix free of heterogeneities such as other fractures or xenoliths. Autoradiographic techniques used in this study were based on Basham (1981). Alpha radiation intensities and distributions were measured using CR39 film as a solid-state alpha particle detector. CR39 is a thermoset polymer plastic used commercially for a variety of eyeglass and eyeshield applications. For alpha autoradiography, CR39 has many practical attributes (Basham, 1981): (i) uniform response to alpha particles up to 6-MeV energy, (ii) optical clarity, (iii) high-resolution recording of alpha impacts, and (iv) ease of development (simple etching).

For autoradiographic measurements, selected polished thin sections were placed face down on CR39 film. Corner locations were marked, and the samples were taped to the CR39 to preclude shifting. Exposure times for the samples varied according to their U contents; the time necessary to produce a measurable pattern was determined by trial and error. For example, sample NOPI-56-TS1 was exposed for 21 days, whereas NOPI-48-TS1 was exposed for 59 days. After exposure, the CR39 film was etched in 6 N NaOH at 80 °C for 2 to 3 hr. The resulting CR39 film contains etch pits, each corresponding to an individual alpha particle impact. The distribution of these alpha impacts was mapped using standard point counting techniques using a Nikon Optiphot-Pol microscope equipped with an ocular micrometer reticule. For each sample, 40 traverses perpendicular to the microfractures were counted, 20 on each side of the microfracture. Counting locations were chosen to avoid other microfractures, xenoliths, or other heterogeneities in the tuff matrix. Counting was extended away from each microfracture until an approximately constant alpha impact density was reached.

3 RESULTS

3.1 GEOLOGIC FEATURES

Clearing and geologic mapping of the Level +10 and +00 surfaces show that the area U mineralization is easily visible on the outcrop, is well-defined, is roughly elliptical in form, and has maximum horizontal dimensions of about 18 m by 30 m. The host rock exposed in the cleared areas, Nopal Formation tuff, has been altered in the vicinity of the deposit. The main secondary minerals observed are kaolinite [$Al_2Si_2O_5(OH)_4$] and iron oxides (variably hematite [Fe_2O_3] and goethite [alpha-FeO · OH]). The abundance of kaolinite tends to increase close to the deposit. Iron oxides tend to be concentrated along fractures, though some highly fractured areas have generally abundant iron oxides.

3.2 CONTACT GAMMA INTENSITY DISTRIBUTION

A total of 1,489 contact gamma measurements was made. Contact gamma mapping of the cleared areas of Levels +10 and +00 showed the highest values to be 28 mR/hr and local background values to be about 0.05 mR/hr. The gamma survey readings are interpreted as proportional to the U concentration because gamma spectrometry of powdered bulk rock samples indicates: (i) thorium concentrations are approximately constant throughout the area (30–50 ppm), (ii) U concentrations vary from 20 to 23,000 ppm in the same area, and (iii) bulk solids are close to secular equilibrium with respect to the ^{238}U and ^{232}Th decay series.

The results of the field gamma survey clearly demarcate the limits of the U mineralization on Levels +10 and +00. A field reading of 1.0 mR/hr corresponds approximately to a bulk rock U concentration of 500 ppm, which is also the apparent limiting value for the presence of U-bearing minerals. The Level +10 exposure of the deposit consists of an interior portion with low-gamma intensity (readings less than 1.0 mR/hr) without apparent U-bearing minerals (i.e., undetected in XRD analysis or by binocular microscopy) and an outer ring 1- to 4-m wide of relatively high-gamma intensity (up to 28 mR/hr) containing abundant, but irregularly distributed, U minerals. Outside the deposit, on Level +10, the gamma intensity drops off quickly. This drop-off in gamma intensity is more abrupt on the western margin than on the northern margin of the deposit. North of the deposit, gamma intensities well above background (4 to 10 times background) extend continuously from the edge of the area of visible U mineralization for about 20 m. On Level +00, gamma intensity drops more slowly with distance from the deposit than on Level +10. This difference is particularly evident to the SE of the deposit on Level +00.

3.3 COMPREHENSIVE FRACTURE MAPPING

Locations, lengths, and forms of 11,374 fractures were mapped. Rock within the deposit area, and the surrounding tuff, is highly fractured (Figure 3-1). Most of the fractures are short (less than 1 m in length) and tend to occur as groups of subparallel breaks. More continuous fissures (i.e., those extending for tens of m) are less common at Nopal I. In general, fractures close to the area of visible U mineralization tend to be more abundant and less continuous than those farther away.

Orientations (strike and dip) of 895 fractures were measured on the cleared areas. These data show that the fractures may be grouped into six major sets (Figures 3-2, 3-3, and 3-4). Most measurements have azimuths within about $\pm$ 30° of EW; fractures with trends closer than 30° to NS are

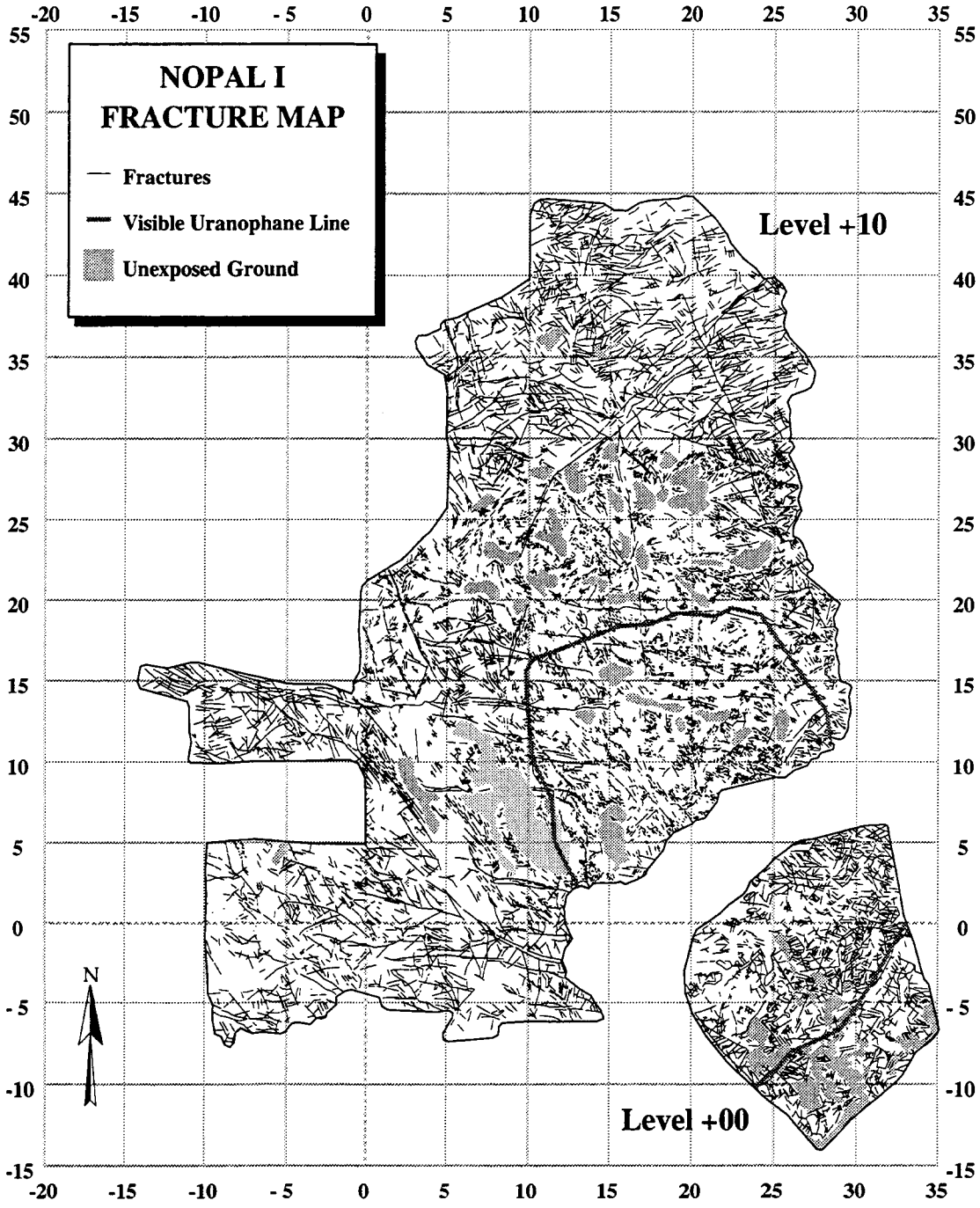

Figure 3-1. Fracture mapping of the Nopal I deposit was carried out at a scale of 1:25. Original field data were digitized and were manipulated using ARC/INFO software. This map includes 11,374 individual fractures. The visible uranophane line indicates the limit of visible U mineralization and marks the nominal edge of the deposit. Level +00 is 10 m lower in elevation than Level +10. The gap between the levels corresponds to the horizontal component of the slope of the face separating the levels and to large debris piles at the base of that face. Perimeter scales are in m.

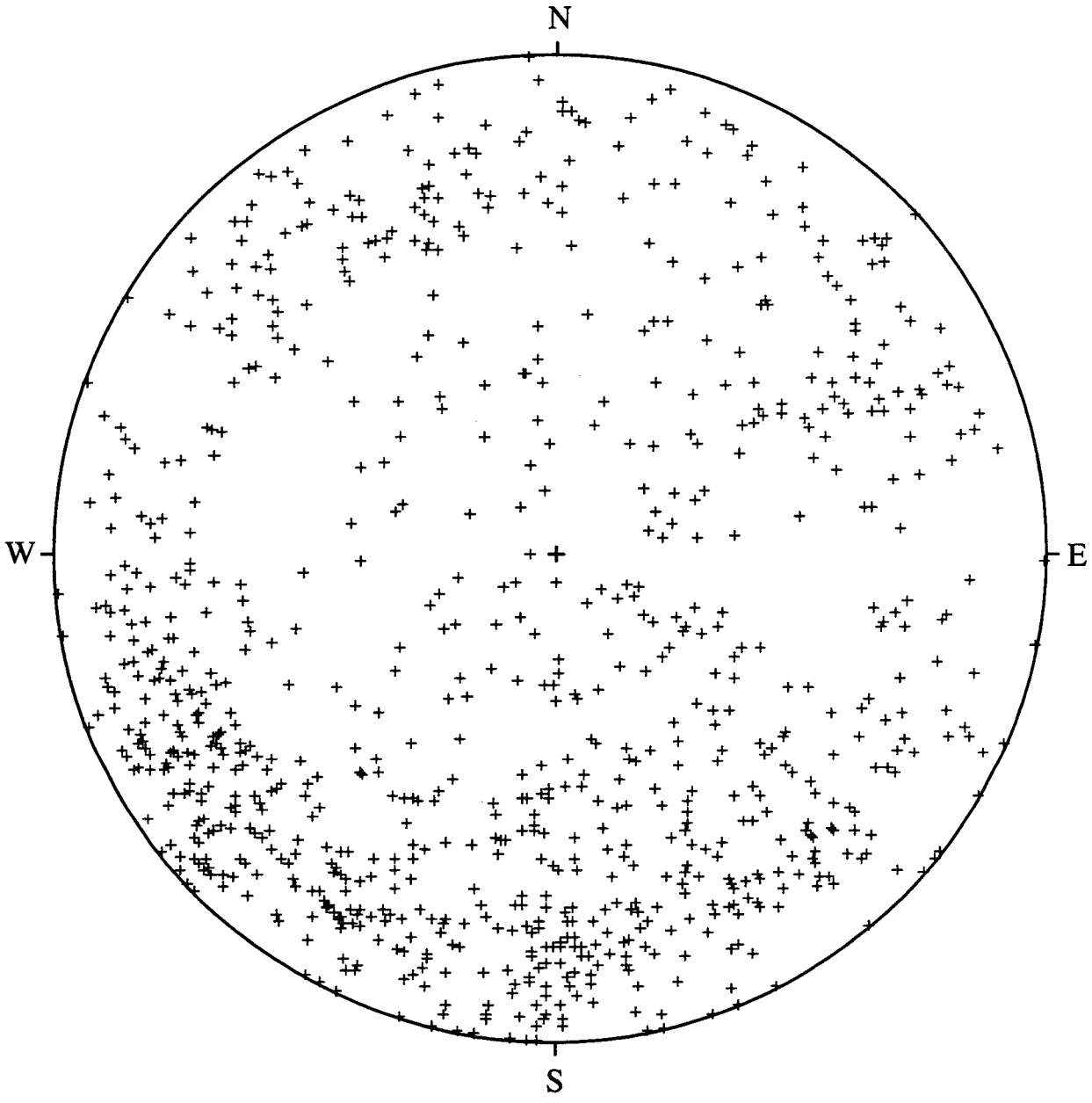

Figure 3-2. Poles to 895 fracture orientations measured on the cleared areas of Levels +10 and +00 are shown here on the lower hemisphere of a Schmidt equal area projection

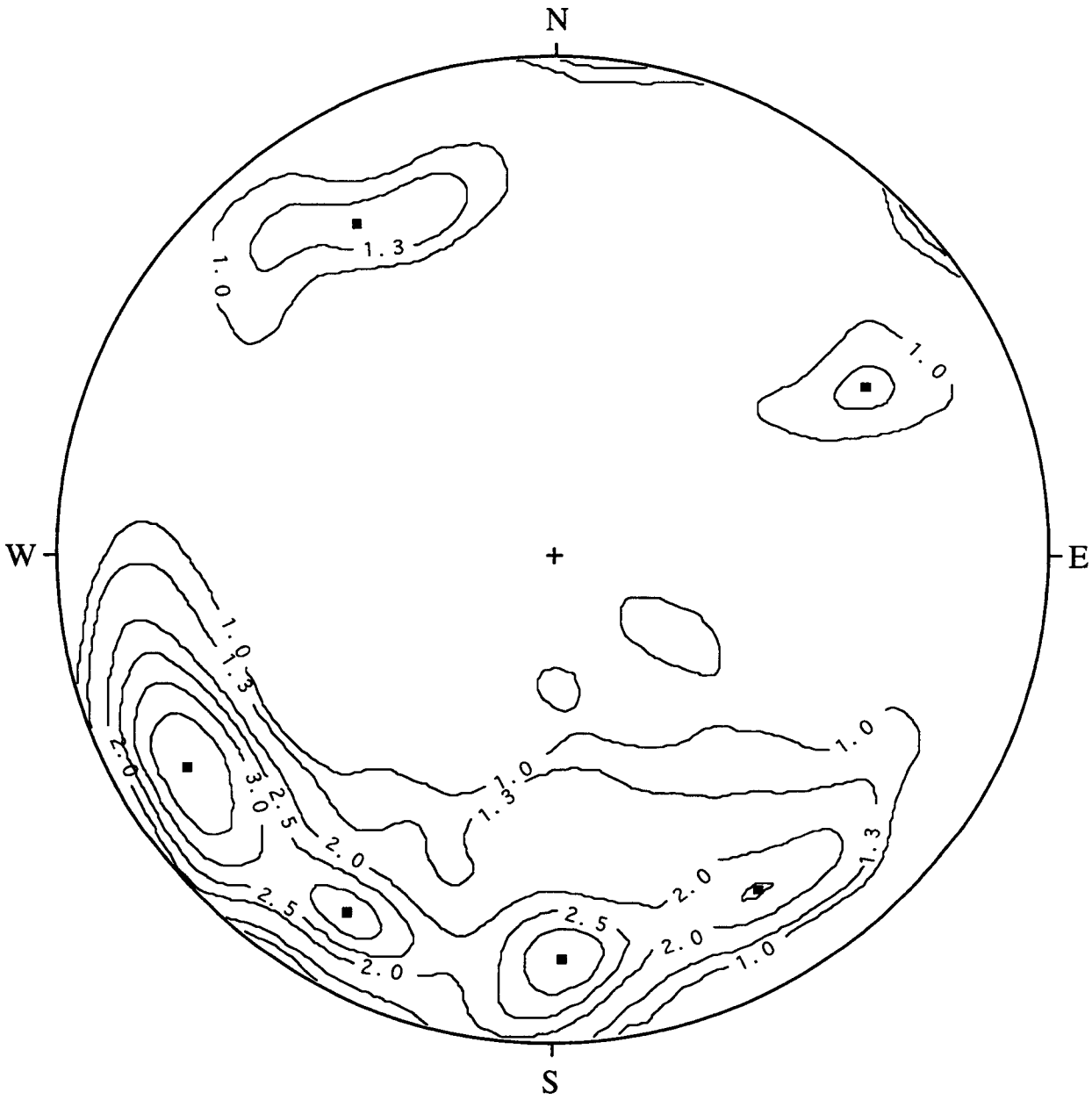

Figure 3-3. Poles to fracture orientations measured on Levels +10 and +00 are contoured here on the lower hemisphere of a Schmidt equal area projection. Density contours of the pole distribution were calculated using a spherical gaussian regression. Contour values indicate percentages of the total dataset (895 measurements). This pattern can be resolved into six central tendencies indicated by the positions of the black squares.

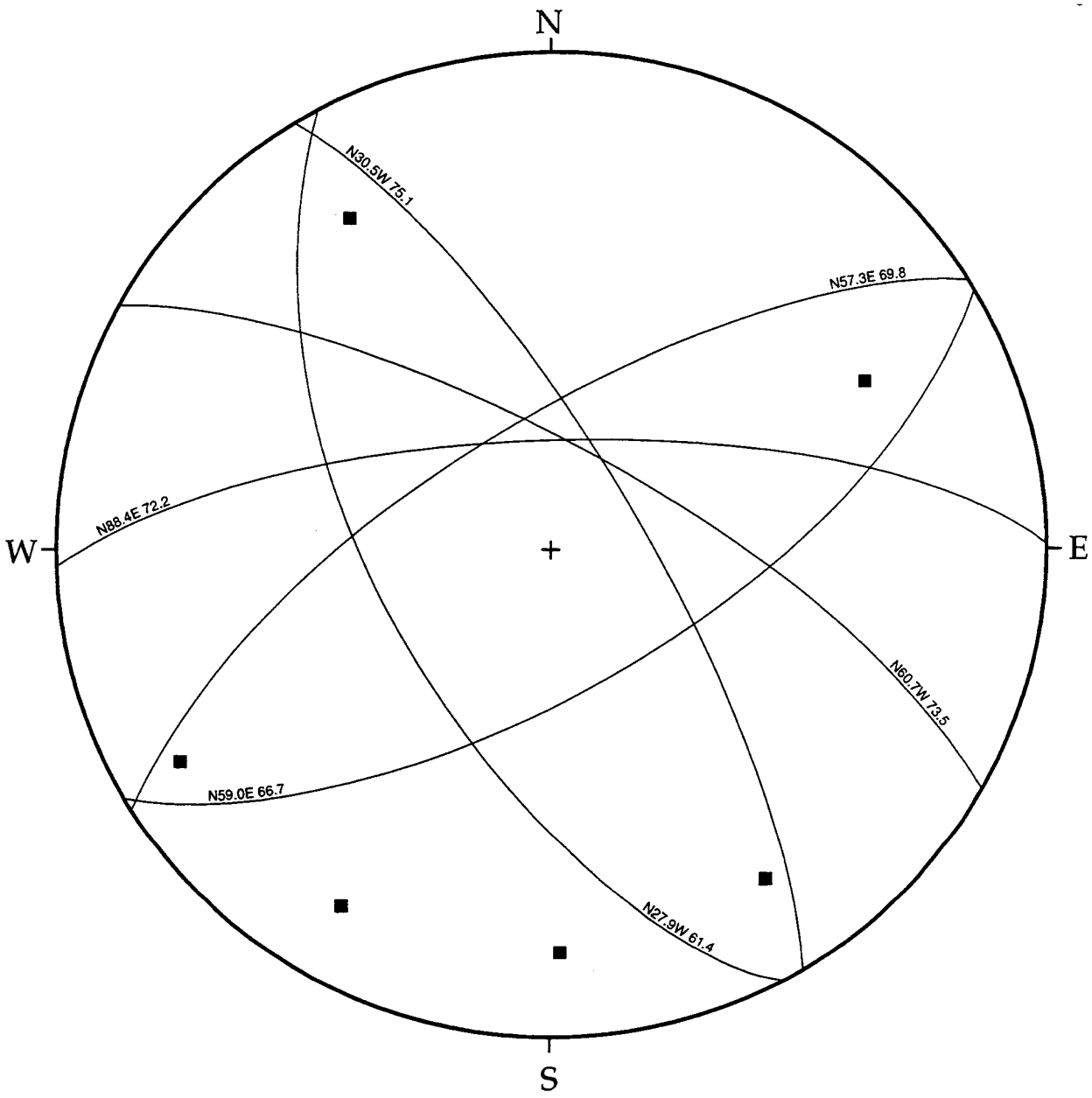

Figure 3-4. This Schmidt equal area projection was constructed using fracture orientations measured on the cleared areas of Levels +10 and +00. This lower hemisphere pattern shows that the complex fracture network at Nopal I is resolvable into six symmetric central tendencies. Curves indicate the strike and dip of each fracture set. Squares indicate the orientation of the pole to each fracture set.

relatively rare at Nopal I. Fractures at Nopal I typically exhibit minor horizontal offsets (e.g., <5 cm). Cross-cutting relationships suggest a relative sequence of formation: (i) NE-trending fractures, (ii) NW-trending fractures, and (iii) EW-trending fractures.

Within the mapped areas, N-dipping fractures are much more abundant than S-dipping fractures (70 percent N-dipping). Both N- and S-dipping fractures tend to have steep inclinations (average dip of 895 fractures is $63.0° \pm 18.5°$ 1 sigma). The lack of low-angle fracture measurements partially represents sampling bias introduced by observations made on an artificially constructed surface that is nearly horizontal and which therefore intersects few fractures with shallow inclinations. Low-angle fractures are, nevertheless, significant features of the Nopal I deposit as evidenced by exposures of undulating, low-angle fissures in vertical faces nearby and some portions of the cleared areas of Levels +10 and +00 with well-developed slickensides. However, only limited observations of low-angle fractures are possible on the cleared areas examined in this study.

3.4 DETAILED STUDY OF A MAJOR FRACTURE SET

The major fracture set at 13.5 m N (Figure 3-5) may be considered a mesofracture (i.e., aperture >1 mm and trace length >10 m). The concentration of U in the 13.5-m N fracture set varies systematically with distance from the deposit. U concentrations in fracture-filling material from the portion of the fracture located within the deposit are quite high (>7 wt% U), and there is a general decrease in the concentration of U in the fracture-filling material with distance from the western edge of the deposit. Close to the deposit (e.g., within 10 m), the concentration of U in the fracture-filling material is 1 to 2 orders of magnitude greater than U concentrations in the bulk tuff at comparable distances from the western boundary of the deposit.

Minerals identified in the 13.5-m N fracture-filling include jarosite [$KFe_3(SO_4)_2(OH)_6$], quartz [SiO_2], goethite [alpha-FeO · OH], hematite [Fe_2O_3], and kaolinite [$Al_2Si_2O_5(OH)_4$]. Jarosite and goethite are the most abundant fracture-filling minerals. The ratio of jarosite to goethite is highest within the deposit and close to the western edge of the deposit (Figure 3-6). The relative proportion of goethite to jarosite increases with distance from the deposit. By about 15 m from the edge of the deposit, jarosite is no longer detected by XRD (XRD may not detect abundances of <5 vol%) but is visible optically as well-formed hexagonal crystals growing into open spaces. Crystalline hematite generally lines open spaces within the fractures. The amount of XRD-detectable hematite increases with distance from the deposit.

3.5 TRANSECTS THROUGH MICROFRACTURED TUFF ADJACENT TO A MAJOR FRACTURE SET

Tuff samples collected along transects perpendicular to the major fracture set at 13.5 m N have a high density of microfractures (i.e., fractures with apertures $<<1$ mm and trace lengths on the order of cm). One-dimensional (1D) fracture density of this rock ranges from 0.54 to 1.65 fractures per cm and averages 1.14 fractures per cm. This value is a minimum for fracture density because it represents only those fractures visible to the unaided eye on the outcrop; a microscopic view would certainly reveal many more fractures (e.g., 10 to 100 times, depending on the scale of observation).

Samples were collected along traverses perpendicular to the 13.5 m N fracture at 0.5, 6.0, 10.2, 15.9, and 20.1 m from the edge of the deposit. These samples show systematic variations in U concentration with distance from the major fracture and with distance from the edge of the deposit.

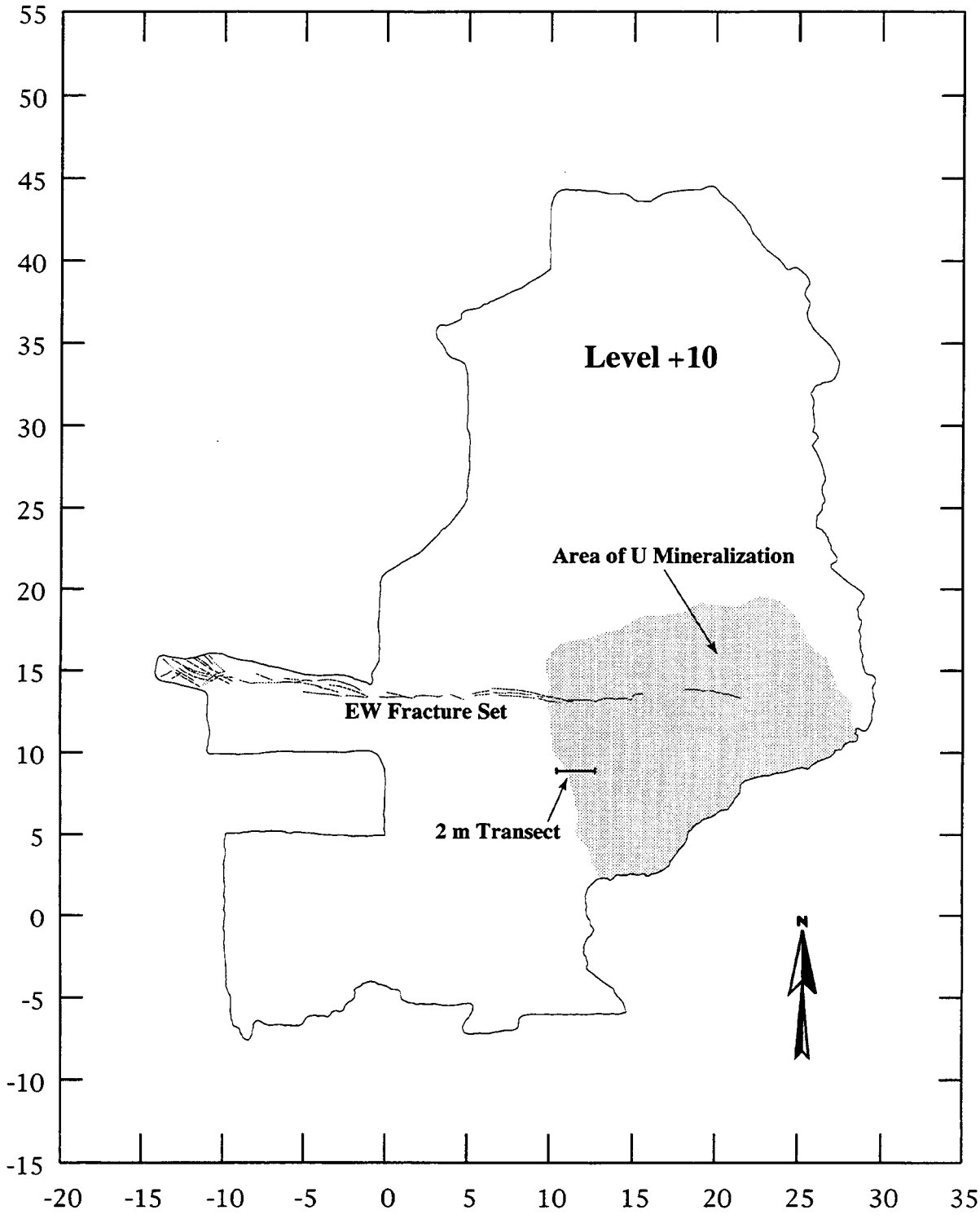

Figure 3-5. This map gives the locations of the major EW fracture set at 13.5 m N and of the 2-m transect across the western margin of the deposit. The pattern of the 13.5-m N fracture set is taken from the fracture map shown in Figure 3-1. Stippled area indicates the portions of Level +10 on which U minerals are visible to the unaided eye. Perimeter scales are in m.

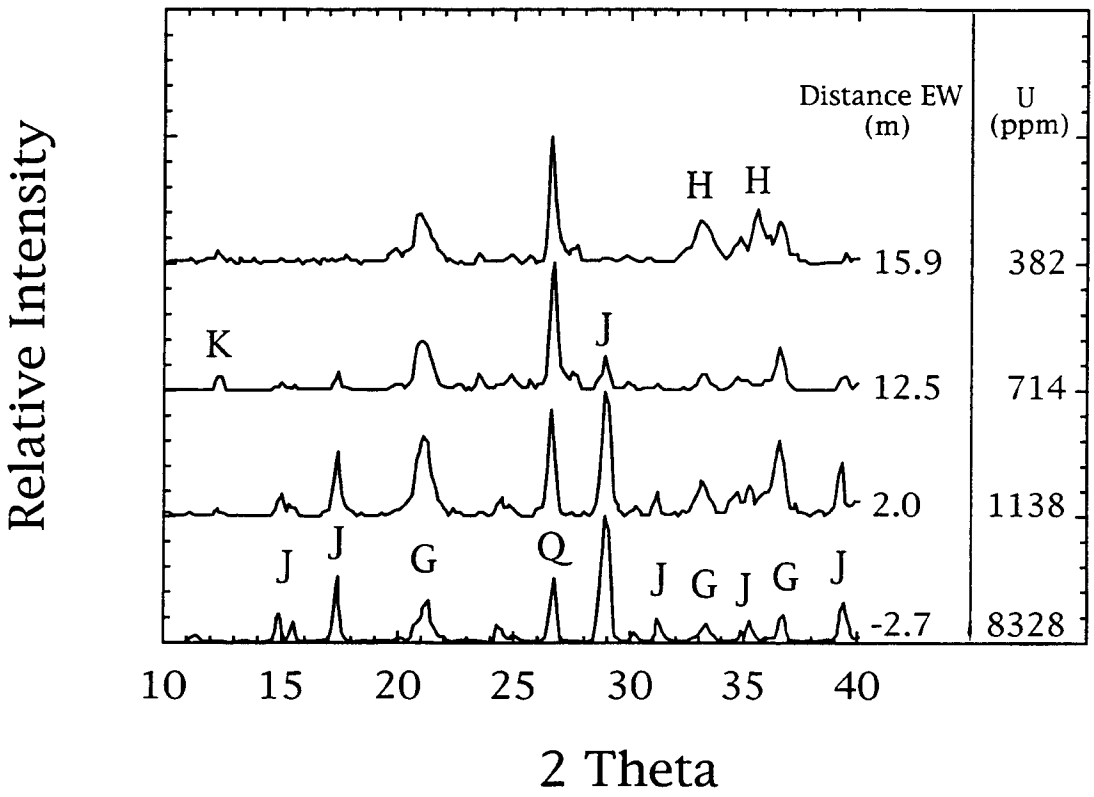

Figure 3-6. X-ray diffractometry patterns of the filling of the major EW fracture set at 13.5 m N collected at varying distance from the edge of the visible U mineralization. The peaks have been normalized to the 100-percent intensity peak for each pattern. Kaolinite (K), jarosite (J), goethite (G), quartz (Q), and hematite (H) were identified. The U concentration of the fracture-filling material and distance from the edge of the deposit are listed next to each pattern.

Samples along a given traverse tend to have progressively lower U concentrations with increasing distance from the major fracture. This general trend is occasionally disrupted by higher or lower U concentrations corresponding to irregularities in the microfracture network through the sample areas. Additionally, U concentrations decrease from traverse to traverse with increasing distance from the edge of the deposit, corresponding to the general decrease in U concentration of the major fracture-filling with distance from the edge of the deposit.

3.6 TRANSECT THROUGH GENERALLY FRACTURED TUFF

U measurements along a 2-m traverse at 9.1 m N (Figure 3-5) show that the transition across generally fractured tuff (i.e., randomly broken on a scale of cm) from the deposit to the unmineralized rock is abrupt and that there appears to be a systematic decrease in the concentration of U away from the area of maximum U concentration (Figure 3-7). Within the zone of visible U mineralization, the concentration of U ranges from about 1,000 to 33,000 ppm (Figure 4-1). Uranyl silicate minerals occur along fracture surfaces of samples collected along this traverse within the deposit; XRD analyses indicate the presence of weeksite [$K_2(UO_2)_2\ Si_6O_{15} \cdot 4H_2O$] in the region of visible U mineralization. Other minerals detected by XRD are quartz, kaolinite, sanidine, and hematite in two samples outside of the area of visible U mineralization. Alpha spectrometry results (Figure 3-8) for the $^{234}U/^{238}U$ activity ratio for

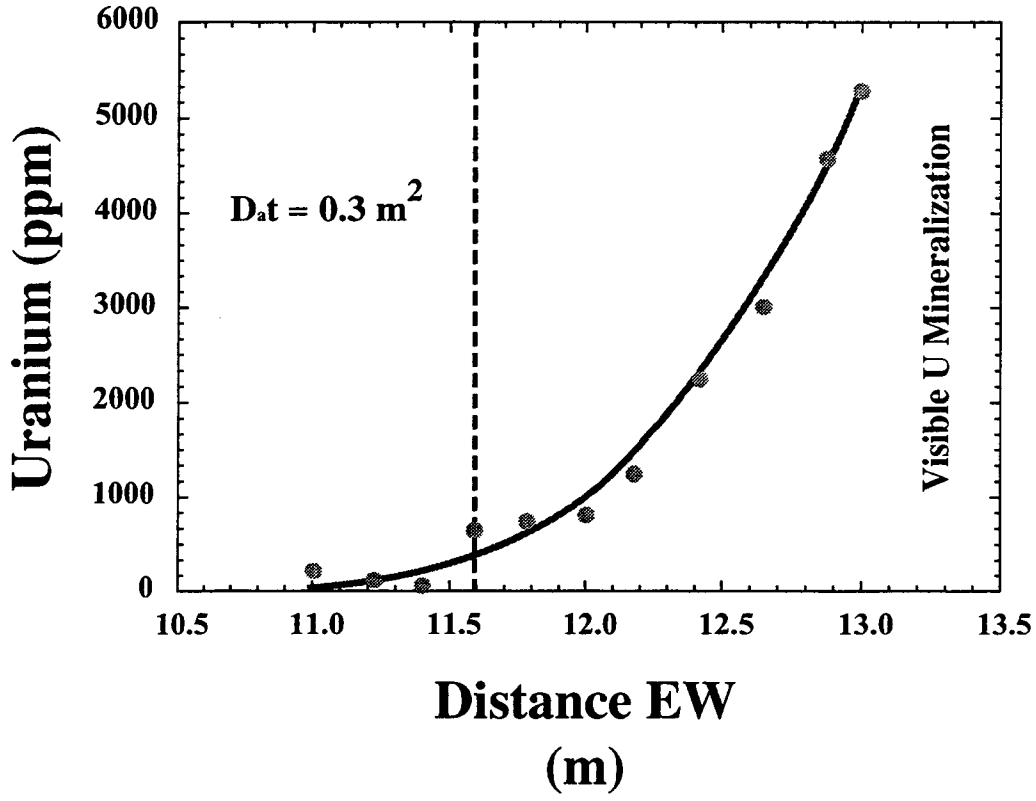

Figure 3-7. This plot shows the U content in bulk rock along a 2-m transect across the western margin of the Nopal I deposit. The solid line is a fit of the diffusion equation to the solid U concentrations using the measured value of 5,282 ppm at 13.0 m East as a boundary condition for U. The dashed vertical line indicates the position of the edge of the visible U mineralization.

samples along this traverse indicate: (i) significant ^{234}U enrichment outside the deposit, indicating that these rocks have been open with respect to U transport processes within the last 1 Ma; and (ii) samples within the deposit are close to secular equilibrium, indicating limited fractional mass transport.

3.7 MICRON-SCALE TRANSECTS IN TUFF MATRIX ADJACENT TO INDIVIDUAL MICROFRACTURES

Variations in the concentration of U in tuff matrix adjacent to individual microfractures were determined using autoradiographic techniques. For these analyses, a direct correspondence was assumed between alpha impacts per unit area per unit time and U content of the sample. There are other alpha emitters in the system in addition to U, including Th and Ra isotopes, which are present as daughters of U. However, U concentrations measured on Level +10 of the Nopal deposit greatly exceed the concentrations of the other alpha emitters; therefore, a direct correspondence between alpha intensity and U contents is a reasonable approximation. Further support for this hypothesis is provided by energy-dispersive x-ray analyses (EDX), including x-ray element mapping, of polished thin sections for which autoradiographic analyses were also conducted. U was the only alpha emitter observed in significant concentrations in these samples.

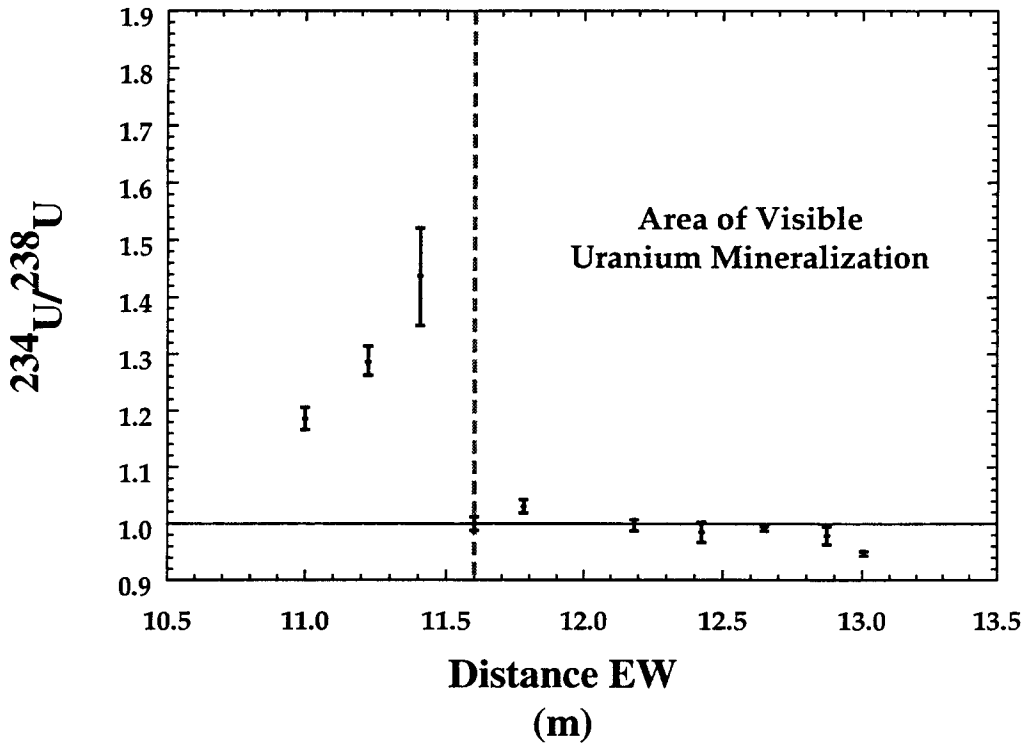

Figure 3-8. This plot shows the $^{234}U/^{238}U$ ratio in bulk rock samples collected along a 2-m transect across the western margin of the Nopal I deposit. These measurements show systematic disequilibrium between ^{234}U and ^{238}U along the profile with a clear increase in $^{234}U/^{238}U$ outside the deposit from near equilibrium values within the deposit. The vertical dashed line indicates the position of the edge of the visible U mineralization.

The resulting alpha distributions are illustrated in Figures 3-9 a,b. Each data point is the result of 40 individual measurements. Raw data for each sample were converted to alpha impacts per unit area per unit time to provide a common basis for comparison. The portion of each curve furthest from the respective microfractures (e.g., from about 0.30 to 0.50 mm) was observed to flatten to an approximately constant value. This value is interpreted to represent the local background U concentration in the tuff adjacent to each microfracture.

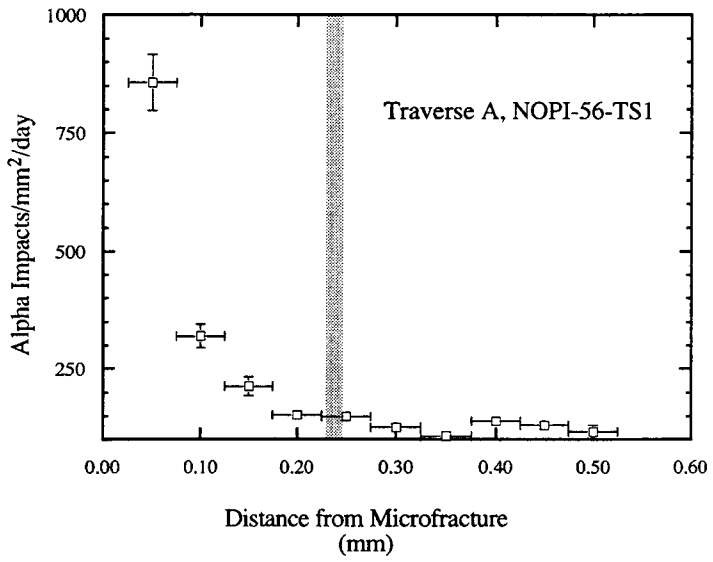

(a)

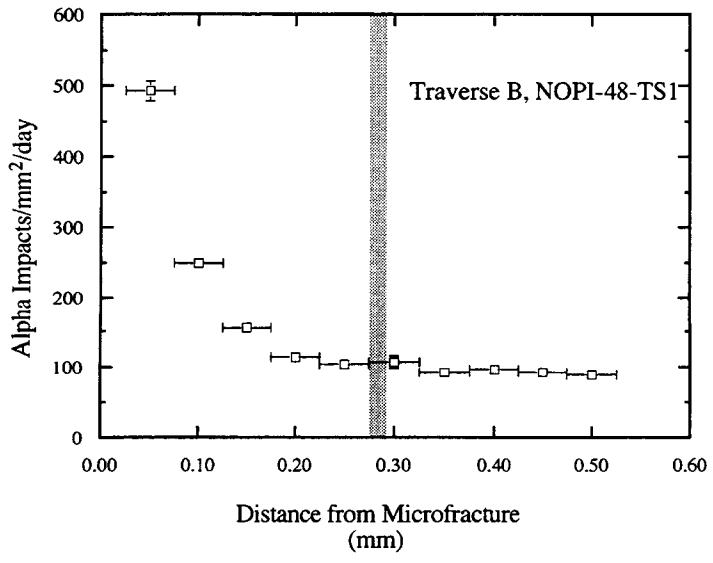

(b)

Figure 3-9. This plot of alpha impact density adjacent to a microfracture is interpreted as a concentration profile of U in the tuff matrix next to the microfracture. Error bars for distance are constant for each measurement and correspond to the distance interval counted for each measurement. Alpha impact density errors are 1 sigma uncertainties. The vertical shaded line indicates the limit of anomalous U concentrations along this profile.

4 DISCUSSION

The Nopal I deposit is interpreted to have formed by hydrothermal solutions that precipitated uraninite (nominally UO_{2+x}) as they moved through a subvertical, highly fractured zone within welded silicic tuff. The youngest of the host rocks (Nopal Formation tuff) has been dated at 43.8 Ma (Alba and Chavez, 1974). The formation of the U deposit is estimated to have occurred about 7.9 $\pm$ 5.2 Ma based on electron microprobe data (Pearcy et al., 1993b). After formation of the primary uraninite, the deposit was altered to a suite of secondary minerals dominated by uranyl oxyhydroxides and uranyl silicates (Pearcy et al., 1993b). It is likely that the secondary U minerals were formed by a combination of hydrothermal and supergene alteration (George-Aniel et al., 1991).

After deposition of the primary uraninite and possible subsequent hydrothermal alteration, the deposit was lifted above the water table by Basin and Range deformation. The deposit was exposed at the surface along the eastern face of a horst (Goodell, 1981). In this position, the deposit has been subject to weathering processes common to the desert areas of northern Mexico [i.e., annual rainfall of about 25 cm (U.S. Department of Commerce, 1965), occurring mostly in episodic downpours]. U-rich caliche located at the elevation of the deposit and about 3 m outside the limit of U mineral occurrence has been dated by U-series isochron techniques at 53.6 $\pm$0.8 Ka (Pearcy et al., 1993b), suggesting that weathering of the deposit has been the dominant mode of alteration for at least that period.

4.1 GENERAL TRANSPORT THROUGH FRACTURED TUFF SURROUNDING THE DEPOSIT

Gamma intensity patterns, mineral distributions, and fracture patterns suggest that U has been remobilized from the area of the original deposit and transported away from the deposit along fracture paths. Geologic mapping of the Nopal I deposit shows that visible U mineralization is limited to a small well-defined area (about 18 m by 30 m). The roughly annular pattern of gamma intensities corresponds to variations in U and non-U mineral occurrence. The limits of the area of U mineralization correspond well to an abrupt decrease in gamma intensity on Level +10 (Figure 4-1), and the interior of the deposit has low-gamma intensity and no observable U minerals. Similarly, XRD analyses of bulk tuff samples from the interior portion of the deposit show abundant alunite [$KAl_3(SO_4)_2(OH)_6$], which is not present in the outer high-gamma intensity ring (Leslie et al., 1993b). On Level +00, gamma intensities greater than 0.45 mR/hr extend well beyond the area of visible U mineralization (Figure 4-1). This extension is most prominent along a SE-trend that corresponds to the downslope direction of the premining surface. Tuff in the area of this extension is heavily weathered to clay (mainly smectite with minor kaolinite). These observations suggest that the greater extent of high U concentrations away from the deposit on Level +00 reflects transport of U away from the deposit in the downslope direction during weathering of the deposit.

The primary ore mineral assemblage of the Nopal I deposit has been shown to be uraninite $\pm$ kaolinite $\pm$ pyrite $\pm$ quartz (Pearcy et al., 1993b). Alteration of primary pyrite by interaction with oxidizing fluids is a likely mechanism leading to formation of the alunite and low pH solutions. Conditions under which alunite forms (oxidizing, low pH) are also conditions that tend to mobilize U. Mobilization of U associated with alunite formation is a probable explanation for the spatial correspondence among low-gamma intensities, the absence of U minerals, and the presence of alunite in the central portion of the deposit.

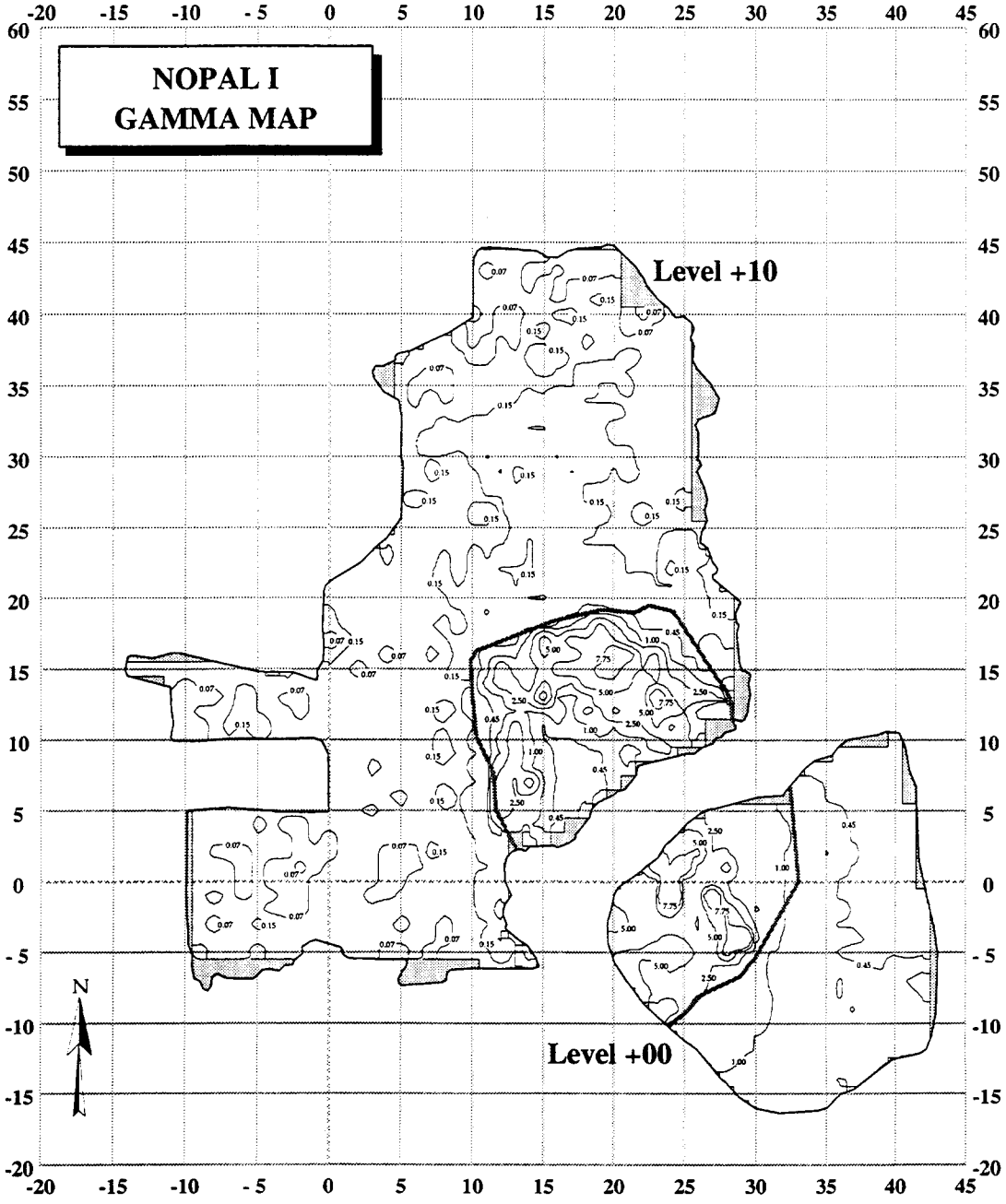

Figure 4-1. This map gives the results of a contact gamma survey conducted of the cleared areas of the Nopal I deposit with measurements made on a 1 m by 1 m grid. The curved, shaded line indicates the limit of visible U mineralization and marks the nominal edge of the deposit. Contours have units of mR/hr. The areas of highest gamma intensity are well defined and, on Level +10, have a semiannular form. Anomalous gamma values are asymmetrically distributed around the deposit with a broader area of high-gamma values extending on Level +10 to the N than to the W and on Level +00 extending preferentially to the SE.

Contact gamma measurements indicate the presence of anomalous U (i.e., U concentrations above local background values) extending to the N of the deposit (i.e., outside the area of visible U mineralization) (Figure 4-1). This N-trending area of anomalous U may represent transport of U from the area of primary deposition. This interpretation is supported by U-series measurements (Leslie et al., 1993a), which have documented a significant U mobilization event at Nopal I at about 54 Ka (see discussion in Section 4.2). If the area of visible U mineralization at Nopal I represents a source area (i.e., the distribution of U prior to subsequent transport), then the N-trending area of anomalous U may be interpreted as the horizontal transport vector along effective flow paths. Using the 0.15 mR/hr boundary (of the continuous area of anomalous U concentrations) as a basis for comparison of transport distances, there is evidence of relatively little transport from the area of visible U mineralization to the W (2 to 3 m maximum), whereas there is evidence of greater transport distance to the N (about 20 m).

There is a strong correspondence between the distribution of anomalous U concentrations to the N of the deposit and the locations of major fractures (i.e., fractures with traces extending more than 10 m). This correspondence suggests that individual major fractures were more important to the long distance (e.g., tens of m) transport of U away from the deposit than was the general fracture network comprising thousands of less continuous fractures. A more detailed discussion of major fracture transport is provided in Section 4.2.

The greater importance of individual major fractures for U transport compared to U transport through the general fracture network is supported by analyses of the general fracture density patterns. Fracture distribution within and around the Nopal I deposit is characterized in two ways (using a 1 m by 1 m grid): (i) as the sum of fracture lengths per square m, and (ii) as the number of fractures per square m. Fracture density by length (i.e., m/m^2) appears randomly distributed across the map area; there is no apparent correspondence to areas of U occurrence (Figure 4-2). This interpretation is confirmed by a lack of significant statistical correlation between gamma intensities and fracture density by length ($r^2 < 0.05$). Therefore, although individual major fractures appear to have been important to U transport, variations in fracture length density (which is insensitive to fracture continuity) do not appear to have been important for U transport. Fracture density calculated by frequency (i.e., number of fractures/m^2) shows a general increase close to the deposit and somewhat higher values N of the deposit (Figure 4-3). This broad correspondence, between fracture density by frequency and gamma intensity, which is apparent upon inspection of the maps, is not supported by a detailed comparison; there is no significant statistical correlation between fracture density by frequency and gamma intensity ($r^2 < 0.02$).

4.1.1 Fractal Analyses

The relationships among U distribution and general fracture patterns are functions of the scale at which the information was collected and analyzed. The scale at which the fractures were mapped and the gamma measurements were made was chosen as the most detailed scale that could be implemented based on practical considerations of available time and resources. Observations and interpretations made at this scale are not necessarily the same as those made at other scales. Fractal analysis of the fracture patterns allows assessment of the scale dependence of the Nopal I fracture network.

The fractal dimension of a pattern is a way of quantitatively expressing the ruggedness of the pattern and has been defined by Mandelbrot (1982) as:

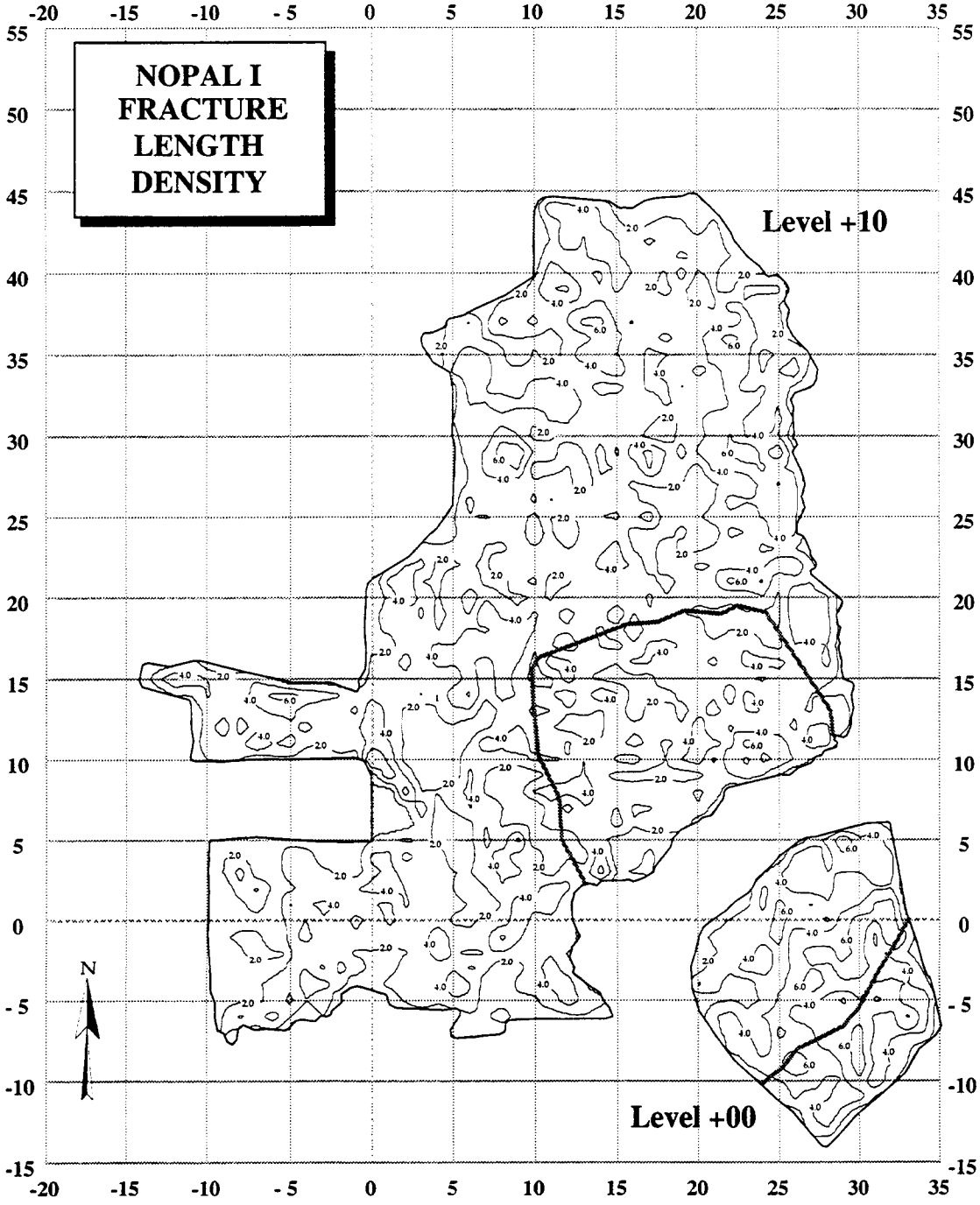

Figure 4-2. This map shows that fracture density calculated by length (i.e., m/m^2) appears randomly distributed across the map area; there is no apparent correspondence to areas of U occurrence. The curved, shaded line indicates the limit of visible U mineralization and marks the nominal edge of the deposit. Contours have units of m of fracture length per m^2.

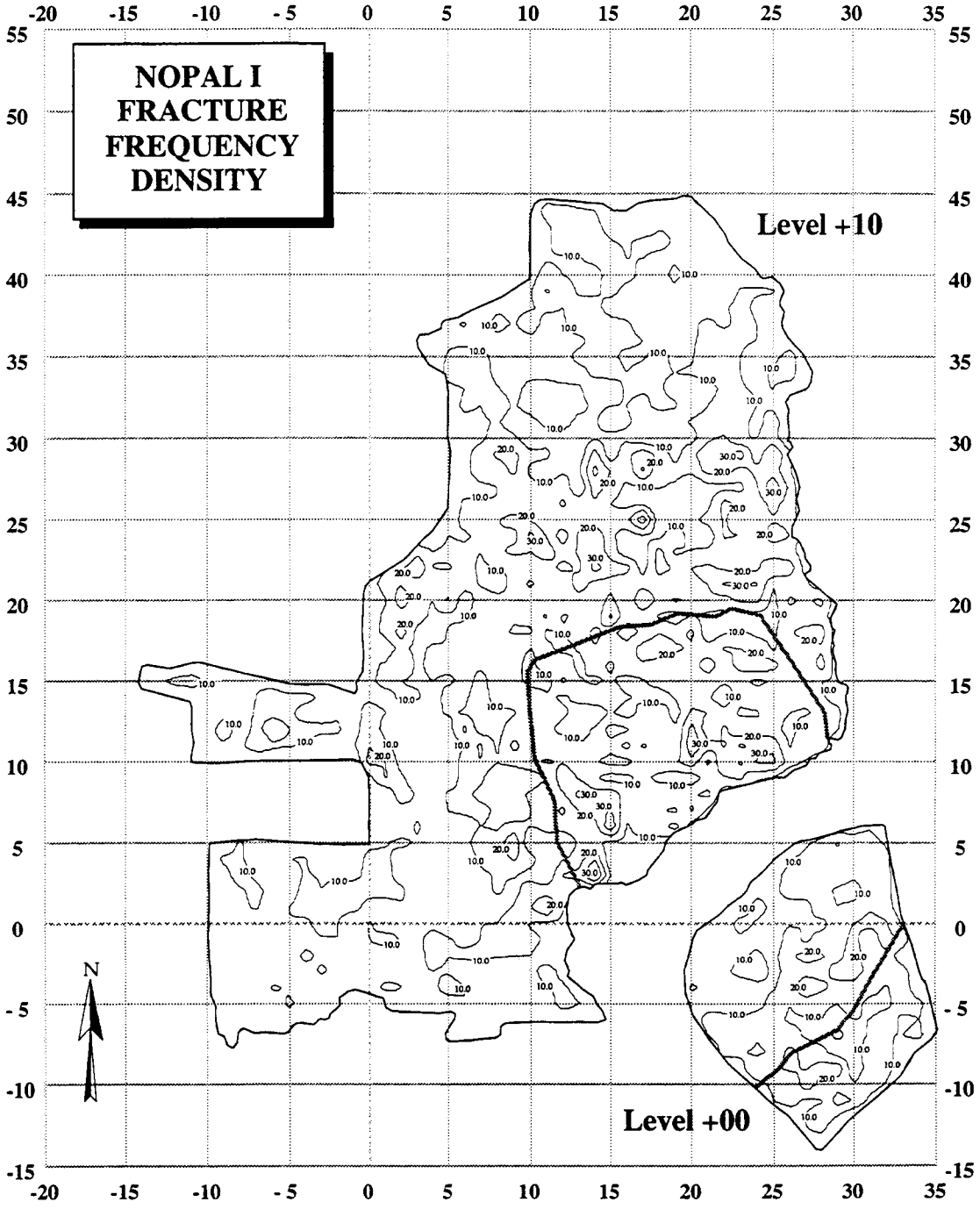

Figure 4-3. This map shows that there is a broad tendency for increased fracture frequency density (i.e., number of fractures/m^2) in the areas close to the Nopal I deposit as opposed to those areas farther away. This broad correspondence is not supported by a detailed comparison; there is no significant statistical correlation between fracture density by frequency and gamma intensity. The curved, shaded line indicates the limit of visible U mineralization and marks the nominal edge of the deposit. Contours have units of number of fractures per m^2.

$$N(R) = R^{-D} \tag{4-1}$$

where D is the fractal dimension of a pattern that can be divided into N intervals of dimension R.

Equation (4-1) describes patterns that are self-similar, that is, the structure of the pattern is scale invariant (Mandelbrot, 1982). Hypothetical, mathematically described patterns may be strictly self-similar whereas natural patterns may be approximately self-similar over some range of scales. For natural patterns, therefore, fractal characteristics may only be true on average; natural patterns may only be statistically self-similar.

The box-counting method of Voss (1988) was used to determine the fractal dimension of the Nopal I fracture pattern. ARC/INFO software was used to calculate square grids with cell dimensions of 1, 2, 3, 4, and 5 m and to count the number of cells (N) of dimension (R) required to cover the entire fracture pattern mapped on Levels +10 and +00. To determine the scale dependence of the fracture interconnectivity, ARC/INFO was first used to identify the locations of fracture intersections; then the same box-counting technique was applied. Evaluation of scale variations in fracture density followed a similar method with the addition of a normalization step. Fracture densities by length and by frequency were considered separately. As the grid cell size changes, the number of fractures (and the total length of fractures) within each cell varies. Comparison of results from different grid sizes requires normalization of each set by the maximum value for any one cell in that grid and by the dimension of the square grid used.

Results are shown in Figures 4-4 to 4-7. In all cases, linear regressions have correlation coefficients (r^2) greater than 0.99. The fracture pattern mapped at Nopal I appears to be a fractal over the range of scales evaluated. The fractal dimension of the fracture pattern is 1.8. Geometrically, the fractal dimension [for two-dimensional (2D) patterns] is bounded $1 < D < 2$; $D = 1$ describes a straight line and $D = 2$ describes a flat plane. Consequently, the fractal dimension may be interpreted as a measure of the complexity of the pattern as it approaches filling the plane (Ghosh and Daemen, 1993). The relatively high value of D for the fracture pattern suggests a statistically complex pattern for the Nopal I fracture distribution (Figure 4-4). The interconnectedness (fracture intersections per unit area) of the fracture pattern also appears to be a fractal (Figures 4-5 and 4-8), though, with a dimension of 1.5, it appears to be less complex than the entire fracture network pattern.

Fracture density distributions may be considered as three-dimensional (3D) patterns with the fractal dimension bounded by $2 < D < 3$ (Ghosh and Daemen, 1993). At Nopal I, both fracture density calculated by frequency (i.e., the number of fractures per unit area) and by length (i.e., the sum of the lengths of the fractures per unit area) are fractals (Figures 4-6 and 4-7). Fracture frequency density has a fractal dimension of 2.4, and fracture length density has a dimension of 2.6.

At scales large (e.g., $> 10^2$ m) or small (e.g., $< 10^0$ m) compared to those evaluated here, the calculated fractal relationships may not hold. However, this analysis suggests some degree of scale independence for the fracture patterns at Nopal I; observations made at a coarse scale may be similar to those made at a finer scale. Further, the statistical self-similarity of this fracture pattern is an important descriptor of the system for comparisons of transport to other systems.

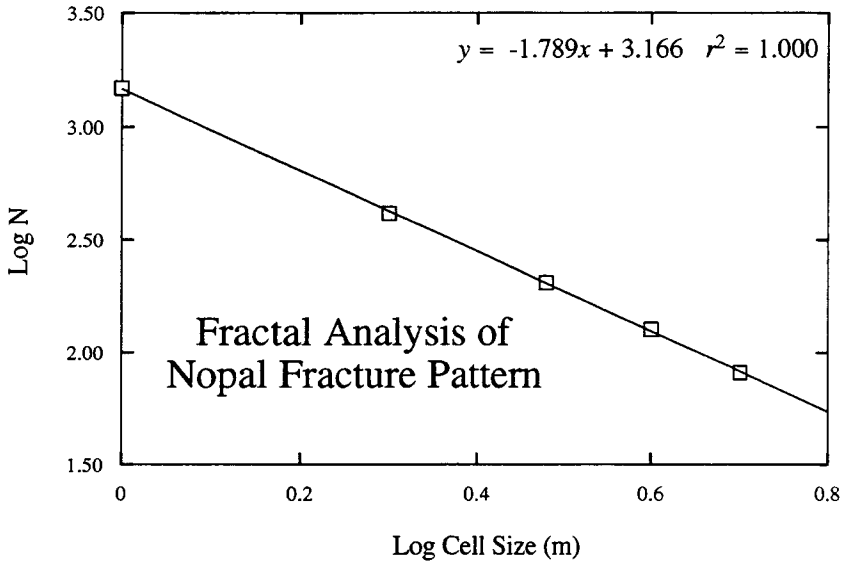

Figure 4-4. Fractal analysis of the Nopal I fracture pattern (i.e., Figure 3-1) shows that the fracture pattern is a fractal. The calculations follow the box-counting method of Voss (1988). Fractal character is demonstrated by a straight line fit (r^2=1.000) to the log of the cell size versus the log of the number of non-zero cells for each cell size (N). The slope of the line gives the fractal dimension of the network (D=1.8).

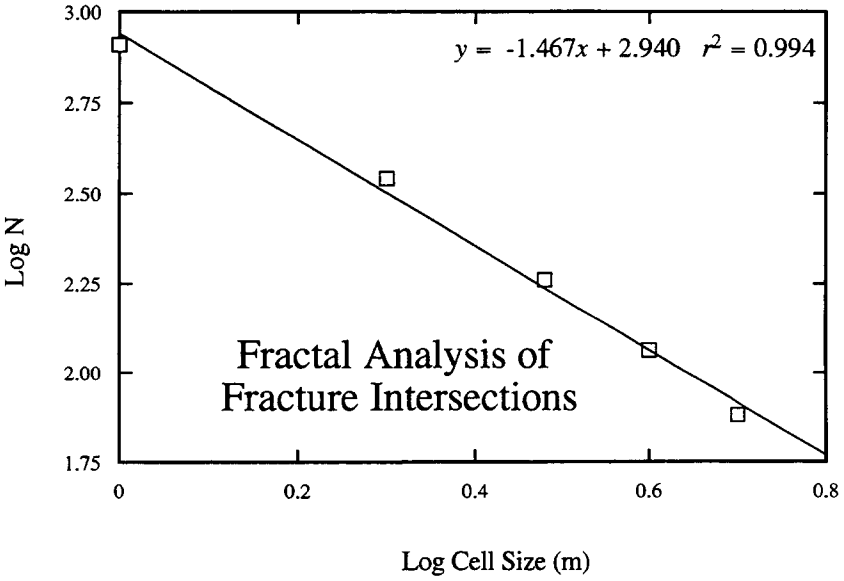

Figure 4-5. Fractal analysis of the interconnectivity of the Nopal I fracture network (i.e., the intersections among fractures illustrated in Figure 3-1) shows that the interconnectivity is a fractal. The calculations follow the box-counting method of Voss (1988). Fractal character is demonstrated by a straight line fit (r^2=0.994) to the log of the cell size versus the log of the number of non-zero cells for each cell size (N). The slope of the line gives the fractal dimension of the network (D=1.5).

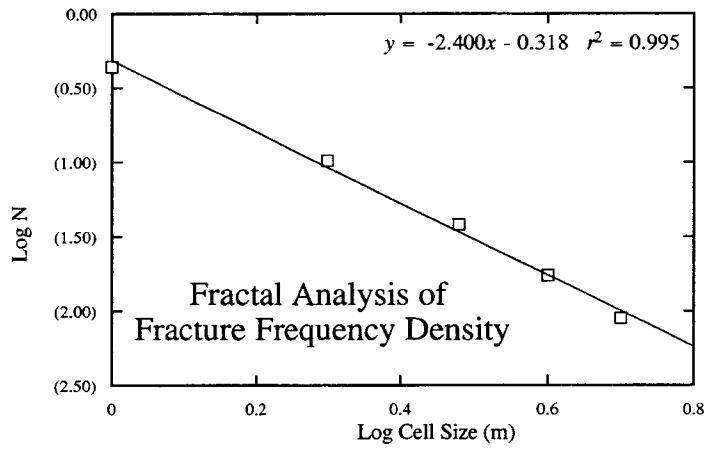

Figure 4-6. Fractal analysis of the fracture frequency density of the Nopal I fracture network (i.e., the number of fractures/m^2) shows that the frequency density is a fractal. The calculations follow the box-counting method of Voss (1988). Fractal character is demonstrated by a straight line fit (r^2=0.995 to the log of the cell size versus the log of the number of non-zero cells for each cell size (N). The number of non-zero cells has been normalized by the maximum value for any one cell in that grid and by the dimension of the square grid. The slope of the line gives the fractal dimension of the network (D=2.4).

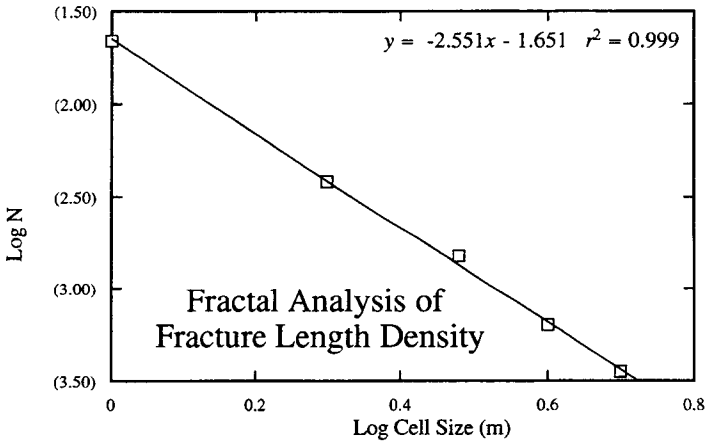

Figure 4-7. Fractal analysis of the fracture length density of the Nopal I fracture network (i.e., the m/m^2) shows that the length density is a fractal. The calculations follow the box-counting method of Voss (1988). Fractal character is demonstrated by a straight line fit (r^2=0.999 to the log of the cell size versus the log of the number of non-zero cells for each cell size (N). The number of non-zero cells has been normalized by the maximum value for any one cell in that grid and by the dimension of the square grid. The slope of the line gives the fractal dimension of the network (D=2.6).

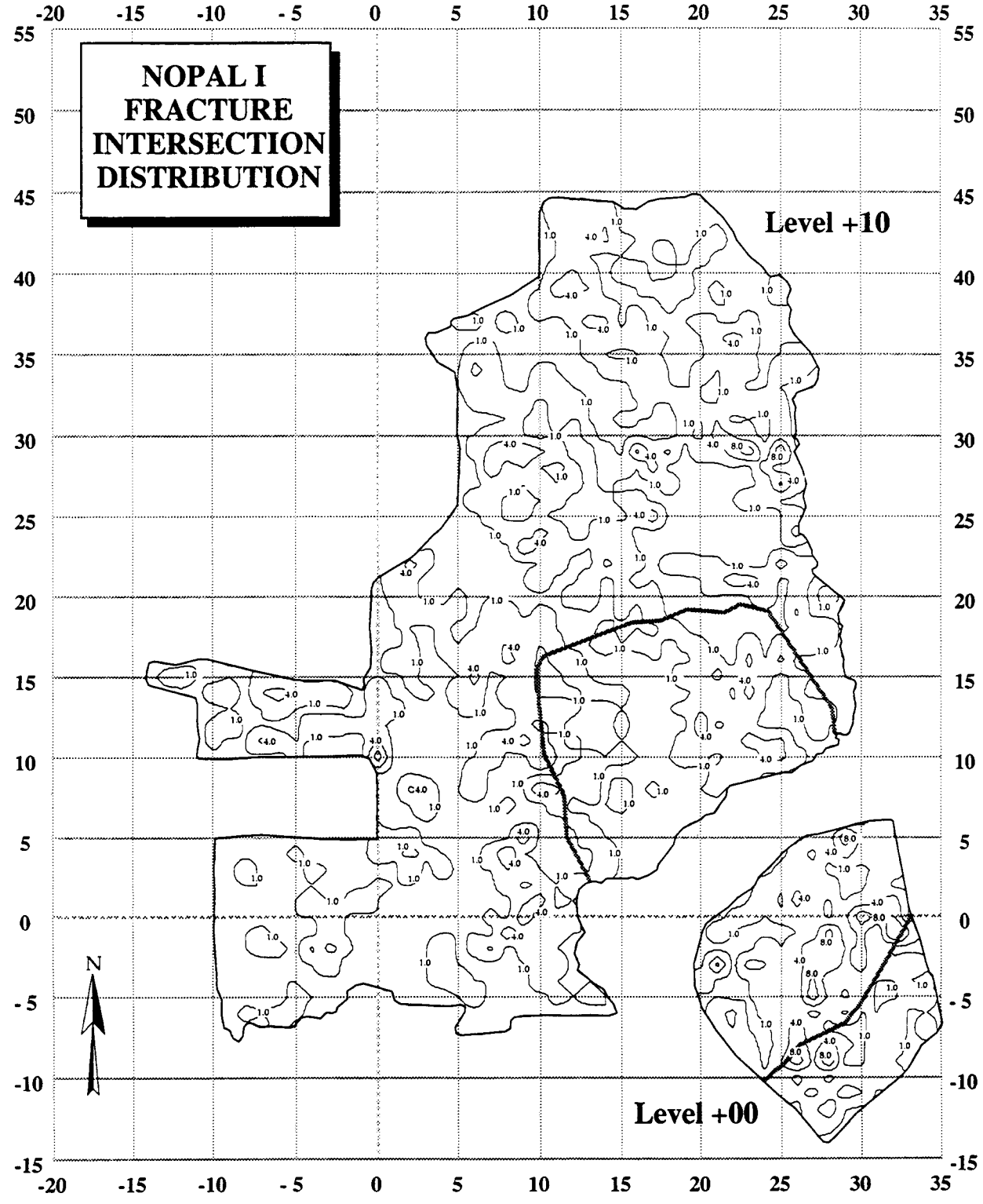

Figure 4-8. The map shows the distribution of intersections among the fractures illustrated in Figure 3-1. The curved, shaded line indicates the limit of visible U mineralization and marks the nominal edge of the deposit. Units are number of fracture intersections per m^2.

4.2 TRANSPORT ALONG A MAJOR FRACTURE SET

The major EW fracture at 13.5 m N intersects the Nopal I deposit and extends across the Level +10 surface to the W (Figure 3-5). The general decrease in U concentration in the filling of the 13.5-m N fracture with increasing distance from the edge of the deposit suggests transport of U away from the deposit (Figure 4-9). This hypothesis is supported by several lines of evidence: (i) structural analysis of relative times of formation among Nopal I fracture sets, (ii) mineralogic gradients within the fracture-filling, and (iii) U-series isotopic measurements.

As described in Section 3.3, EW-trending fractures at Nopal I, of which the fracture at 13.5 m N is one, are structurally the most recent among the various fracture sets at the site. Further, the 13.5-m N fracture is observed to cross cut the U deposit itself; that is, the 13.5-m N fracture forms a physical discontinuity within the deposit not offset by internal features of the deposit, indicating that the fracture is younger than the U deposit. Therefore, it is unlikely that U was transported along the 13.5-m N fracture toward the deposit during primary accumulation of U. Formation of the 13.5-m N fracture after accumulation of the U deposit presents a geometry in which the fracture extends from tuff outside the deposit where U concentrations are about 10 ppm to within the deposit where U concentrations average about 1,100 ppm (George-Aniel et al., 1991). This concentration gradient, present at the time of formation of the 13.5-m N fracture, is more likely to have resulted in movement of U away from the deposit than toward the deposit.

The mineralogical composition of the fracture-filling material offers additional constraints on the transport of U in the 13.5-m N fracture. Notably, XRD indicates that the amount of jarosite in the fracture-filling diminishes with distance from the deposit. Jarosite occurs most commonly in acidic, sulfate-rich environments developed as a result of pyrite [FeS_2] oxidation during weathering (Nordstrom, 1982). The primary mineral assemblage of the Nopal I deposit has been established as uraninite $\pm$ kaolinite $\pm$ pyrite $\pm$ quartz (Pearcy et al., 1993a). The occurrence of pyrite within the deposit and the absence of high concentrations of S or U in the host rocks outside the deposit (Pearcy et al., 1993a) suggest that the deposit itself was the source of both the S in the jarosite and the U in the fracture-filling. Although both the U content of the fracture-filling and the quantity of jarosite decrease with distance from the deposit, it is unlikely that jarosite is directly responsible for this U distribution because jarosite tends not to sequester U (or Th) during its formation (Dickson and Herczeg, 1992).

U-series isotopic measurements have documented significant U transport around the deposit during the last 1 Ma with a specific event dated at about 54 Ka (Leslie et al., 1993a). As described in Section 3.6, tuff samples collected in generally fractured tuff along a 2-m transect across the western margin of the deposit show U-series disequilibria, indicating U transport outside the deposit during the last 1 Ma. This 2-m transect is approximately parallel to the 13.5-m N fracture and located about 4.4 m to the S. Paragenetically late, U-rich opal collected from the deposit about 5 m S of the 13.5-m N fracture has been dated by U-series techniques at 54.3 $\pm$ 2 Ka. U-series dating of a U-enriched caliche collected from a remnant of the pre-mining surface located about 30 m S of the 13.5-m N fracture also indicates significant U transport at 53.6 $\pm$ 8 Ka. This evidence of relatively recent remobilization of U previously accumulated in the deposit is consistent with transport away from the deposit.

Anomalous U concentrations have been measured along the 13.5-m N fracture for a distance of 23.2 m outside the Nopal I deposit. A linear projection of the generally decreasing values outside the limit of the deposit predicts that background values would be reached at 26.3 m from the deposit edge

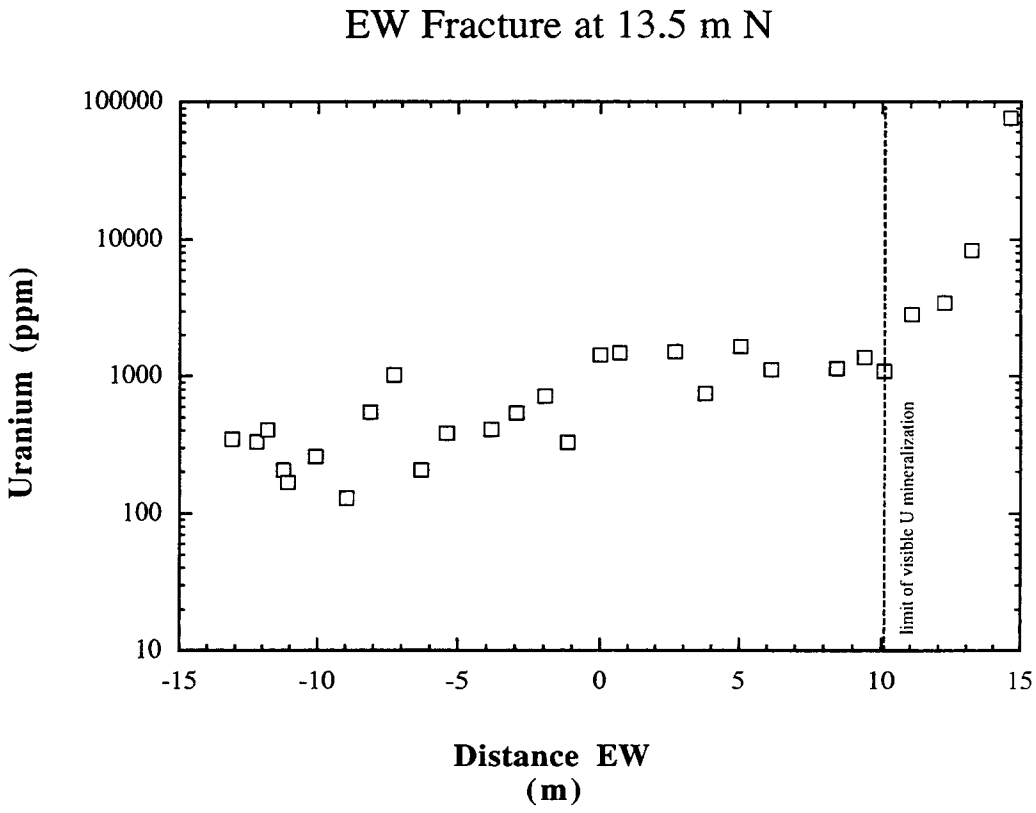

Figure 4-9. Concentration of U in the fracture-filling material along the major EW fracture at 13.5 m N. The vertical dashed line indicates the edge of the Nopal I deposit. Uncertainties in U concentration are much less than the plot symbol size.

(Figure 4-10). This distance is comparable to the maximum extent of anomalous U concentrations measured by contact gamma survey (described in Sections 3.2 and 4.1), which are also interpreted to be a result of U transport along major fracture paths.

The decrease in U content along the 13.5-m N fracture away from the deposit could be due to chemical interaction (e.g., sorption), or chemical reaction (e.g., pH increase) of the U-transporting fluid with the wall rock, or differences in the nature of the interaction of the fluid with the wall rock due to varying composition/mineralogy of the bulk rock with distance from the deposit [e.g., George-Aniel et al. (1991); Ildefonse et al. (1990b)]. As discussed in Section 4.1, alteration of the primary ore mineral assemblage appears likely to have produced an oxidizing, low pH solution capable of transporting U away from the area of original deposition and out along the 13.5-m N fracture. The decrease in U concentration in the fracture-filling material with distance may reflect reaction of such a fluid with the fracture wall rock.

It is interesting to note that the anomalous U within the 13.5-m N fracture is not reflected in the general gamma intensity map of Level +10 (Figure 4-1). This is because contact gamma measurements were made at the intersections of the 1 m by 1 m sample location grid lines described in Section 2.0. Since the 13.5-m N fracture lies between the 13-m N and the 14-m N lines, the fracture was missed in the gamma survey. Additionally, though the U concentrations in the 13.5-m N fracture-filling

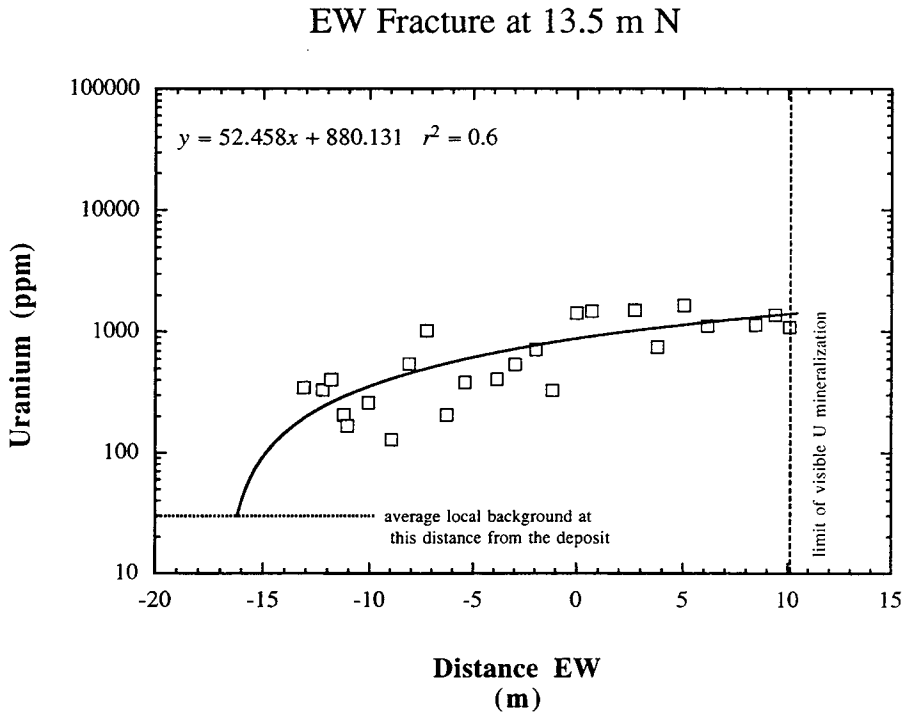

Figure 4-10. This plot shows the concentrations of U in the fracture-filling material along the major EW fracture at 13.5 m N outside the edge of the Nopal I deposit. A linear fit to these data predicts the concentration of U of the fracture-filling will reach local background levels (about 30 ppm) at 26.3 m from the edge of the deposit. Uncertainties in U concentration are much smaller than the plot symbol dimension.

are anomalously high, for most of the fracture length the concentrations are close to or below the limits of detection of the field gamma meter used for the survey.

4.3 TRANSPORT THROUGH MICROFRACTURED TUFF

As described in Section 3.5, the U content of the microfractured (i.e., fractures with apertures $<<1$ mm and lengths on the order of cm) rock enclosing the major EW fracture at 13.5 m N was measured along five traverses perpendicular to the major fracture (at distances 0.5, 6.0, 10.2, 15.9, and 20.1 m away from the edge of the deposit, Figures 4-11 and 4-12 and Table 4-1). U concentrations along these traverses were found to drop off steeply with distance from the major fracture. However, the drop-off patterns contain irregularities corresponding to the presence of microfractures in the rock. These microfractures form a complex network through which the major EW fracture forms a near-vertical, subplanar discontinuity. The microfracture network appears responsible for transporting U away from the major fracture into the enclosing microfractured tuff, thereby inhibiting the transport of U away from the deposit along the major fracture.

U concentrations along each of the five perpendicular traverses drop off steeply and flatten with distance from the major EW fracture as the concentration approaches local background values (Figures

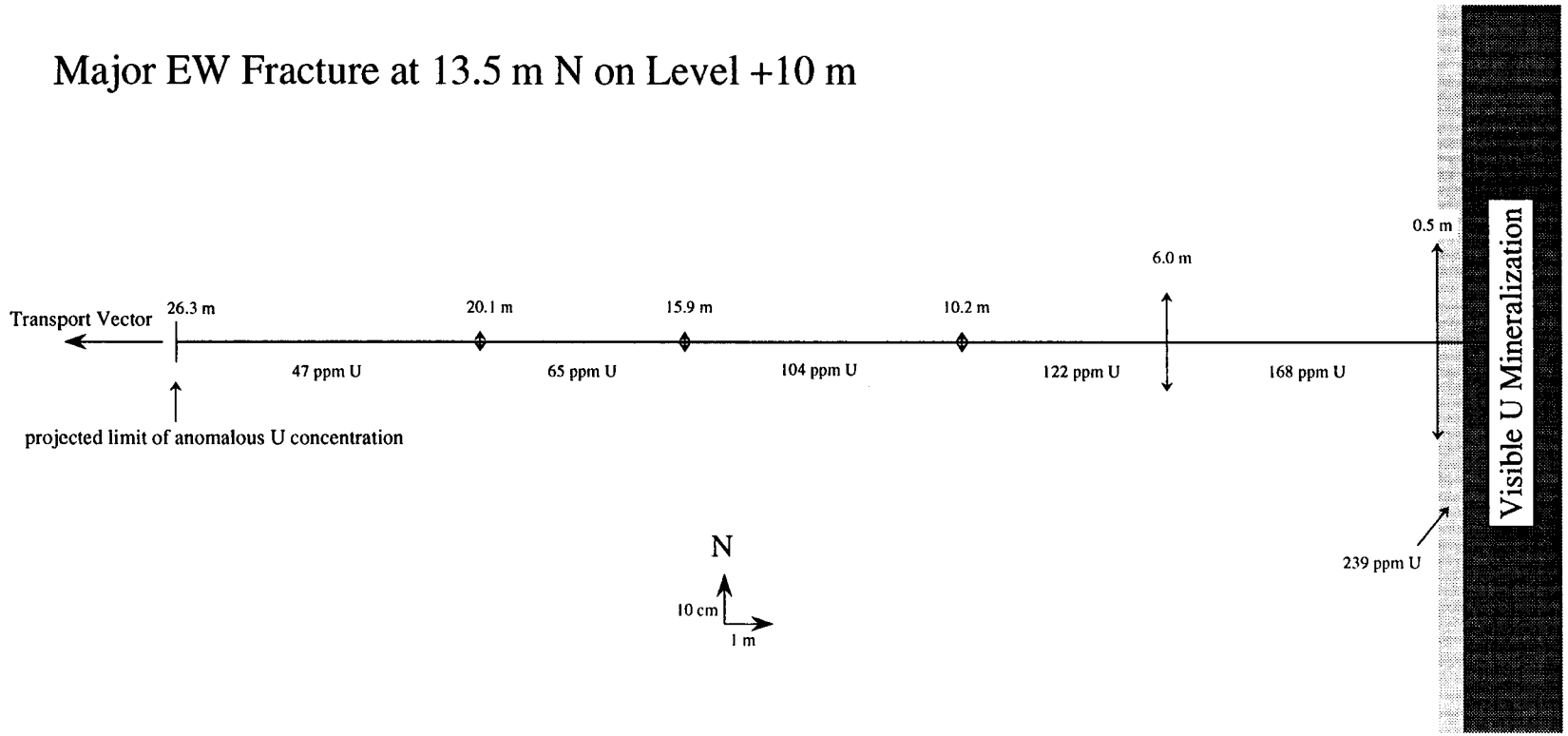

Figure 4-11. This drawing schematically illustrates the spatial relationships among the major EW fracture at 13.5 m N, the sample transects collected perpendicular to the fracture, and the edge of the Nopal I deposit. NS arrows give the distances of anomalous U concentrations from the major fracture; locations for each traverse are the distance from the edge of the deposit. U concentrations are given as the average for the microfractured areas N and S of the major fracture for each interval. Note that the drawing is scaled so that distances NS are expanded 10 times compared to distances EW.

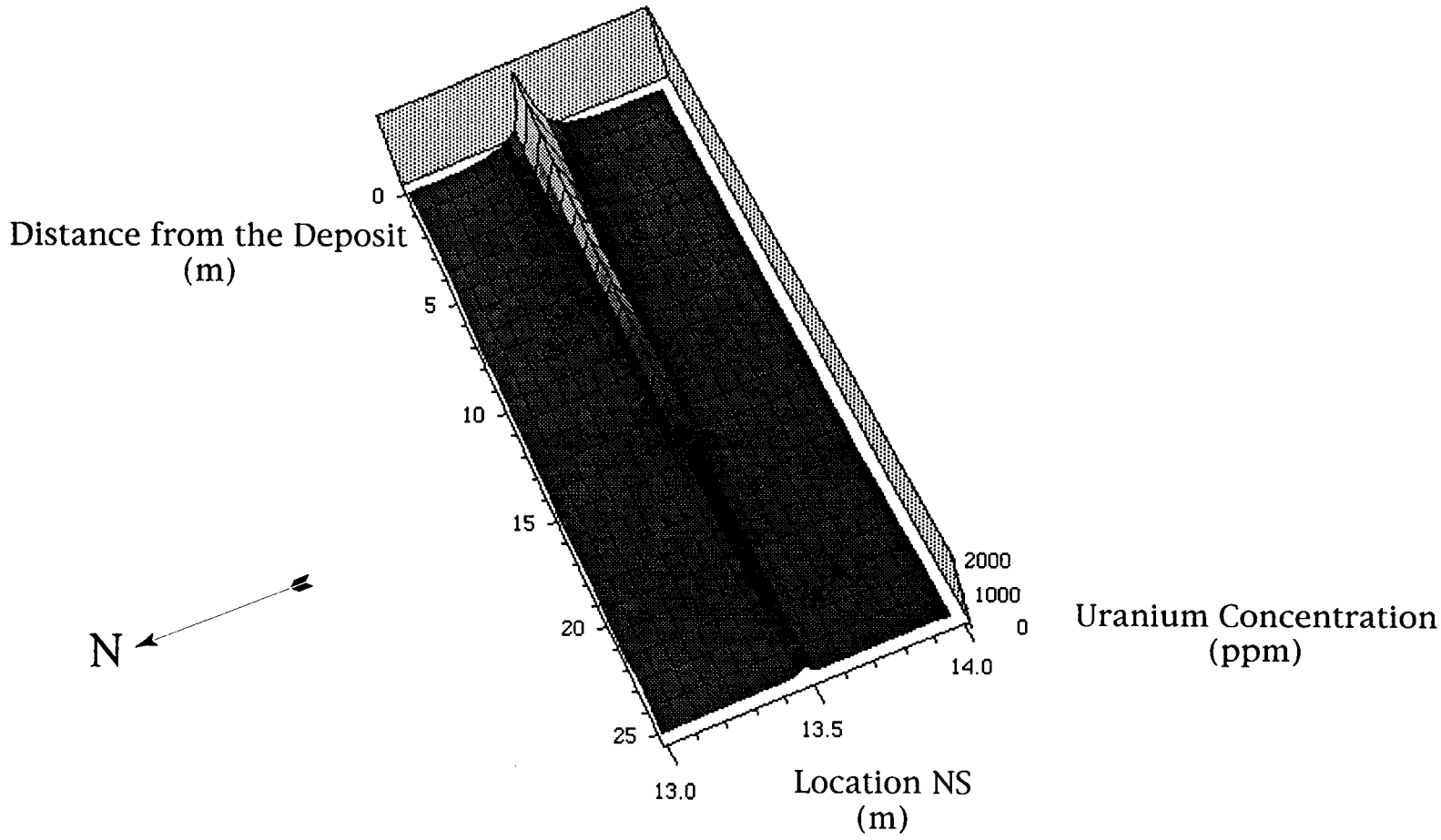

Figure 4-12. This model schematically illustrates variations in U concentrations along the major fracture at 13.5 m N and along transects perpendicular to the major fracture (i.e., Figure 4-11). Note that distances NS are expanded about 12 times compared to distances EW. Data which this surface approximates are given in Table 4-1.

Table 4-1. Uranium content of microfractured tuff measured along traverses perpendicular to the EW fracture at 13.5 m N

Traverse at 0.5 m From Deposit Edge[1]		Traverse at 6.0 m From Deposit Edge[1]		Traverse at 10.2 m From Deposit Edge[2]		Traverse at 15.9 m From Deposit Edge[3]		Traverse at 20.1 m From Deposit Edge[2]	
Distance Interval from Fracture (cm)	Uranium Concentration (ppm)	Distance Interval from Fracture (cm)	Uranium Concentration (ppm)	Distance Interval from Fracture (cm)	Uranium Concentration (ppm)	Distance Interval from Fracture (cm)	Uranium Concentration (ppm)	Distance Interval from Fracture (cm)	Uranium Concentration (ppm)
0.00 to 3.00	**898.70**	**0.00 to 3.00**	**205.90**	0.05 to 0.53	177.40	0.25 to 0.61	110.60	0.00 to 0.84	67.90
0.00 to 3.00	315.10	0.00 to 3.00	150.70	0.73 to 0.85	109.30	0.81 to 0.99	43.50	1.04 to 1.21	72.70
3.00 to 6.00	**213.10**	**3.00 to 6.00**	**48.43**	1.05 to 1.31	87.95	1.19 to 1.35	36.50	1.41 to 1.62	62.50
3.50 to 7.50	175.90	3.50 to 7.50	77.76	1.52 to 1.72	102.70	1.55 to 1.75	32.20	1.82 to 2.02	52.60
7.50 to 13.50	**146.10**	**6.00 to 9.00**	**38.57**	1.92 to 2.12	104.00	1.95 to 2.51	35.62	2.22 to 2.41	46.64
9.00 to 12.00	158.00	10.50 to 14.50	64.32	2.32 to 2.48	126.70	—	—	—	—
13.50 to 19.50	**84.84**	**10.00 to 13.00**	**38.40**	2.67 to 2.91	128.50	—	—	—	—
12.00 to 15.00	130.40	14.50 to 18.50	70.48	3.11 to 3.19	112.50	—	—	—	—
28.50 to 31.50	**91.65**	—	—	—	—	—	—	—	—
37.00 to 33.00	134.85	—	—	—	—	—	—	—	—
46.50 to 53.50	**53.36**	—	—	—	—	—	—	—	—
46.50 to 53.50	124.69	—	—	—	—	—	—	—	—

[1]Traverses at 0.5 and 6.0 m were collected both N (bold) and S of the EW fracture
[2]Traverses at 10.2 and 20.1 m were collected S of the EW fracture
[3]Traverse at 15.9 m was collected N of the EW fracture

4-13a to 4-13e). Discernment of the distance from the major EW fracture at which local background U concentration is reached is complicated by irregularities in the U concentration patterns corresponding to local microfractures. Because of these uncertainties, the limits interpreted for these traverses are minimum distances; the actual area around the major EW fracture into which anomalous U penetrated may be somewhat larger than that estimated here. The limit of likely influence of U transport from the major EW fracture into the microfractured tuff was chosen as the limit of continuous decrease in U concentration (Figures 4-13a to 4-13e).

The distance from the major EW fracture at which the local background concentration is approached is approximately constant at distances greater than 10 m from the deposit. At 20.1, 15.9, and 10.2 m from the deposit, background values are approached at about 2 cm from the major EW fracture. As the distance from the deposit decreases from 10 m, the distance at which the background concentration is approached increases. At 6.0 m, anomalous U concentrations extend to about 10 cm, and, at 0.5 m from the edge of the deposit, anomalous U concentrations extend about 20 cm from the major EW fracture. The proximity of the 0.5-m traverse to the edge of the deposit complicates this interpretation; some of the U measured along the 0.5-m traverse may have moved directly W out of the deposit rather than W along the major fracture and then out N and S along the 0.5-m traverse. Based on measurements along the 2-m transect at 9.1 m N (Section 3.6), this directly transported contribution could be significant (e.g., 100 ppm). Nevertheless, the steep decrease in U concentration along the first 20 cm of the 0.5-m traverse is a clear indication of microfracture transport out of the major EW fracture for at least that distance. The systematic variation in transport distance from the major fracture out into the microfractured tuff is consistent with the increase in U concentration in the major EW fracture-filling approaching the deposit margin.

4.4 TRANSPORT THROUGH GENERALLY FRACTURED TUFF

As described in Section 3.6, U concentrations along a 2-m traverse across the W margin of the deposit at 9.1 m N vary systematically (Figure 3-7), suggesting U transport away from the deposit. This possibility is supported by $^{234}U/^{238}U$ ratios along the same path which show approximate secular equilibrium within the deposit and increased ^{234}U outside the deposit (Figure 3-8). ^{234}U tends to be concentrated in water because of alpha recoil and radiation damage. The ^{234}U enrichment outside the deposit along this traverse, suggests that water with an elevated 234/238 ratio allowed migration out of the area of visible U mineralization into the surrounding tuff where the 234-enriched U was then deposited. The ^{234}U depletion within the area of visible U mineralization is indiscernible because of the large mass of U relative to the small fraction that has been removed.

U concentrations in the bulk rock along the 2-m traverse at 9.1 m N can be fit by a classical diffusion equation. For 1D steady-state flow in homogeneous saturated media, general transport is described by the advection-dispersion equation:

$$\frac{\partial C_{aq}}{\partial t} = \underbrace{\frac{D\partial^2 C_{aq}}{\partial x^2}}_{\text{dispersion term}} - \underbrace{\frac{\rho \partial C_{sol}}{\theta \partial t}}_{\text{source term}} - \underbrace{\frac{V_{aq}\partial C_{aq}}{\partial x}}_{\text{advection term}} \qquad (4\text{-}2)$$

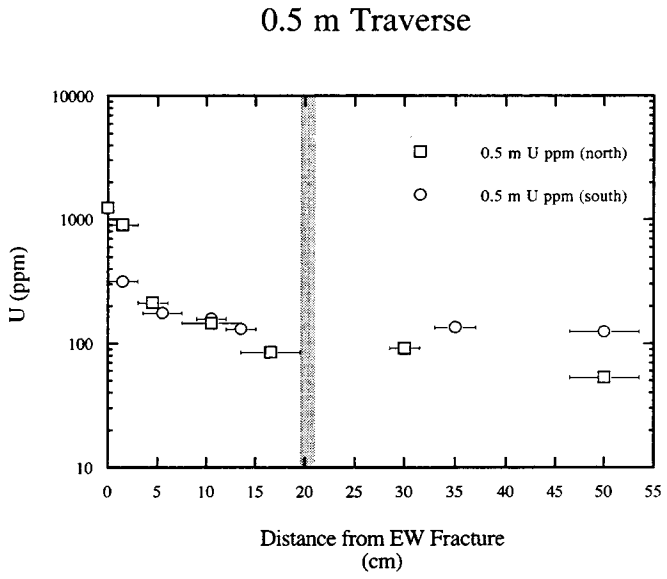

(a)

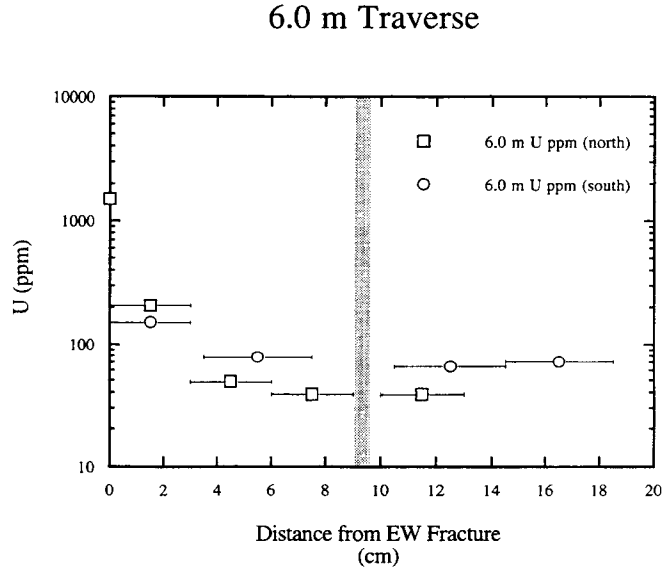

(b)

Figure 4-13a,b. These plots show variations in U concentration with distance perpendicular to the major fracture at 13.5 m N. These profiles are also illustrated in Figure 4-11. Uncertainties in U concentrations are much less than the dimension of the plot symbols. Error bars for distance indicate the distance interval spanned by each sample (i.e., the length of the sample in that direction). Shaded lines indicate the interpreted limits of anomalous U concentration for each traverse. These limits were selected to be likely minima for each traverse. Data for these plots are given in Table 4-1.

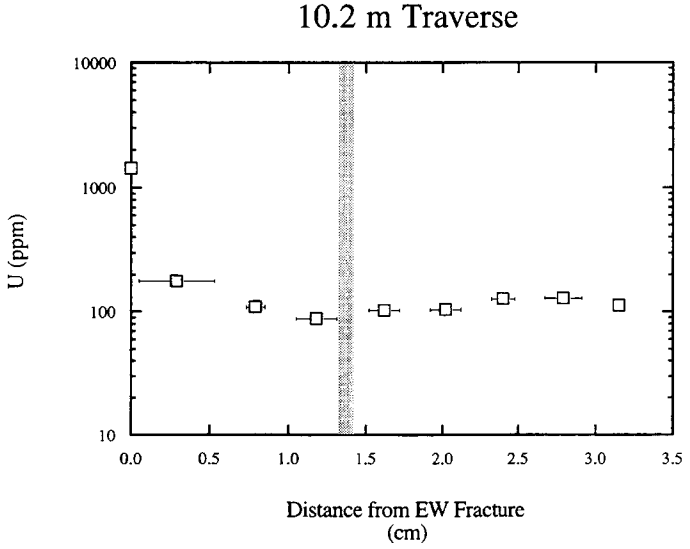

(c)

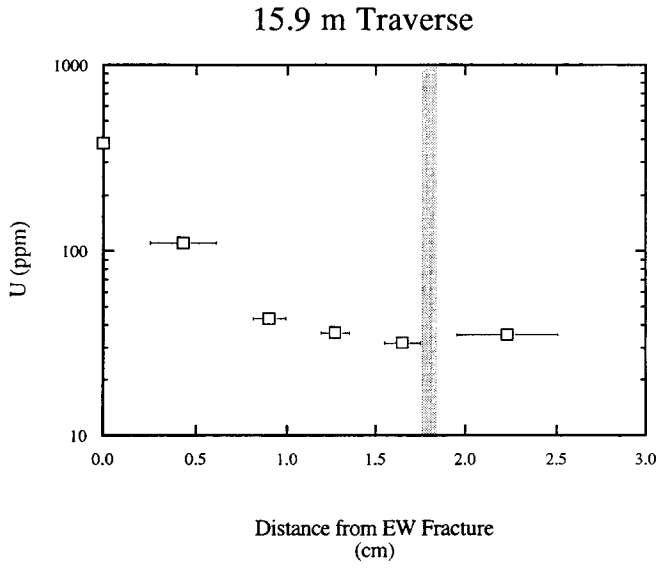

(d)

Figure 4-13c,d. These plots show variations in U concentration with distance perpendicular to the major fracture at 13.5 m N. These profiles are also illustrated in Figure 4-11. Uncertainties in U concentrations are much less than the dimension of the plot symbols. Error bars for distance indicate the distance interval spanned by each sample (i.e., the length of the sample in that direction). Shaded lines indicate the interpreted limits of anomalous U concentration for each traverse. These limits were selected to be likely minima for each traverse. Data for these plots are given in Table 4-1. (cont'd)

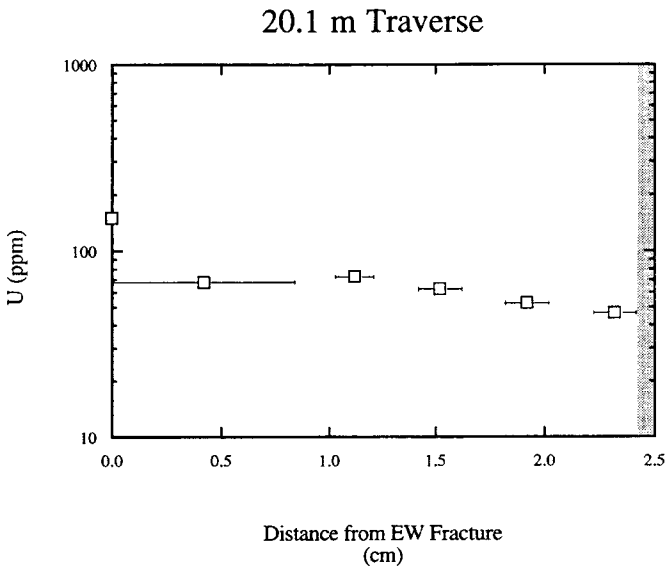

(e)

Figure 4-13e. This plot show variations in U concentration with distance perpendicular to the major fracture at 13.5 m N. These profiles are also illustrated in Figure 4-11. Uncertainties in U concentrations are much less than the dimension of the plot symbols. Error bars for distance indicate the distance interval spanned by each sample (i.e., the length of the sample in that direction). Shaded lines indicate the interpreted limits of anomalous U concentration for each traverse. These limits were selected to be likely minima for each traverse. For the 20.1-m traverse, the limit is not clear and was chosen to be the end of the traverse. This uncertainty has only a small effect on U inventory calculations because of the low U content at that distance from the deposit. Data for this plot are given in Table 4-1. (cont'd)

where:

C_{aq} = concentration in the aqueous phase

D = dispersivity (α) + molecular diffusion (D_a)

x = distance

t = time

ρ = bulk mass density of the porous medium

C_{sol} = mass adsorbed on solid per unit mass solid

θ = porosity

$\overline{V}_{aq}$ = average linear velocity of the aqueous phase

Considering the source term and the advection term to be zero, Eq. (4-2) reduces to Fick's second law:

$$\frac{\partial C_{aq}}{\partial t} = \frac{D_a \partial^2 C_{aq}}{\partial x^2} \tag{4-3}$$

For the following boundary conditions $C(x,t)$:

$$C(x,0) = 0 \quad \text{for } x > 0$$
$$C(\infty,t) = 0 \quad \text{for } t \geq 0$$
$$C(0,t) = C^\circ \quad \text{for } t \geq 0$$

integration of Eq. (4-3) gives:

$$\frac{C_{aq}}{C^\circ_{aq}} = 1 - erf\left[\frac{x}{2\sqrt{D_a t}}\right] \tag{4-4}$$

In this solution, D_a includes several factors:

$$D_a = D_v \frac{\theta \delta}{\tau^2 K_d} \tag{4-5}$$

where:

D_v = diffusivity in water

θ = porosity

δ = constrictivity

τ = tortuosity

K_d = volumetric sorption equilibrium constant

Equation (4-4) describes 1D diffusion in a semi-infinite medium with a constant concentration boundary condition (Neretnieks, 1980). It should be noted that the chemical data measured here are concentrations in the solid not concentrations of dissolved solutes, although transport is presumed to occur in the aqueous phase. The present calculation assumes the measured concentrations in the tuff represent the concentrations of U formerly present as mobile, diffusing species. For these calculations, the constant concentration boundary condition was taken to be the U concentration at 13.0 m E. Fitting the measured profile to the diffusion equation allows estimation of either the molecular diffusion D_a (if the time for the diffusion process is known), or the time t necessary to generate the diffusion profile (if the molecular diffusion of the dissolved species is known). In this case, however, neither is known. Therefore, the fit of the diffusion equation to the profile results in an estimate of the product $D_a t$.

U concentrations along the 2-m profile can be fit to the diffusion equation of a solute through a porous medium if the product $D_a t$ is about 0.3 m^2 (Figure 3-5). This use of the diffusion equation to model solid phase U bulk concentrations assumes that the distribution coefficient (K_d) for U between the solid and aqueous phases is a constant, that the media through which the U diffused had uniform hydrologic properties, and that there was no advection. This simple linear relationship between concentrations of U in the bulk rock and the postulated fluid concentration could be explained by a linear K_d sorption model (e.g., Turner, 1991). It should be strongly emphasized that modeling of the data from this profile is only tentative and that further analysis (petrographic, mineralogic, chemical, and theoretical) is required to evaluate any implications of the model for performance assessment sorption/transport modeling.

4.5 MATRIX TRANSPORT PERPENDICULAR TO MICROFRACTURES

Samples chosen for measurement of matrix transport were collected within the area of the deposit on Level +10. Microfractures within these samples contain relatively high concentrations of U, largely as uranophane [$Ca(UO_2)_2Si_2O_7 \cdot 6H_2O$]. U within the microfractures was transported in the aqueous phase. From the measured concentration profiles, it appears that a portion of the U within the microfractures was transported out of the microfractures into the matrix of the host tuff.

Mineralogic and geometric comparisons of the sample profiles find them to be generally comparable but to have differences that may be significant for U transport (Figures 3-9 a,b). Optical microscopy indicates that the mineralogic composition of the matrix of both samples is similar (fine grained to cryptocrystalline quartz, feldspar, and kaolinite). The matrix of sample NOPI-56-TS1, however, contains significant iron oxide, which is absent from sample NOPI-48-TS1. Nominal apertures of the microfractures in the two samples are also different. The microfracture in sample NOPI-56-TS1 has an aperture of about 100 μm, whereas sample NOPI-48-TS1 has a microfracture width of about 230 μm. The samples were collected about 5 m apart. The higher alpha intensity close to the microfracture of sample NOPI-56-TS1 is consistent with its location in a higher U area of the deposit relative to sample NOPI-48-TS1. General U abundances and alteration mineral distributions suggest that these locations may have had different alteration histories (Leslie et al., 1993b).

Given these differences (iron oxide content of the matrix, aperture widths, U concentration close to the microfractures, and apparent alteration histories), it is interesting that the maximum extent of excess U in the solid for each sample is comparable; the maximum extent of excess U in the matrix appears to be 0.23 to 0.28 mm (distance measured perpendicular to the microfractures). This similarity of maximum extent of excess U in the matrix may indicate insensitivity to the differences listed above or may result from a balance of competing effects produced by the differences. For example, sample NOPI-56-TS1 has the higher U source concentration, hence a stronger concentration gradient (which would tend to extend the U transport distance). However, it also has a greater iron oxide content in the surrounding matrix [which would tend to restrict transport as U is sorbed onto hydrated iron oxides (Guthrie, 1991)]. The similarity in U profiles may also indicate that the measured U transport away from the microfractures is a product of earlier or later events than those which produced the difference in gross alteration histories for the two locations.

Allowing the closest measurement point to the microfractures to approximate a constant concentration boundary condition, the U profiles measured for NOPI-56-TS1 and NOPI-48-TS1 can be fit closely by the classical diffusion model described in Eq. (4-5) (Figures 4-14a,b). Because neither the diffusion coefficient (D_a) nor the time over which the diffusion may have occurred (t) is known, the model can only be solved for the product $D_a t$. Sample NOPI-56-TS1 produces a best fit $D_a t$ of 1.5×10^{-3} mm^2, whereas sample NOPI-48-TS1 has a $D_a t$ of 2.5×10^{-3} mm^2. This difference may result from disparities in the effective local diffusion coefficient and/or the time over which diffusion occurred. However, uncertainties illustrated on Figures 4-14a,b suggest that the small difference in estimated $D_a t$ may not be significant.

4.6 RELATIVE EFFECTIVENESS OF MESOFRACTURE, MICROFRACTURE, AND MATRIX RETARDATION AND RETENTION OF URANIUM

Using the measurements discussed in earlier sections, it is possible to estimate the relative effectiveness of mesofracture, microfracture, and matrix retardation and retention for U transport at the Nopal I deposit. Consideration of the U contents retained in these three areas allows a ranking of effective retardation. It is possible that additional U was transported along these paths and not retained (though there is no evidence for that). Nevertheless, U content estimates provide a basis for comparison among the three types of retardation measured at the site.

The major fracture at 13.5 m N has a trace length greater than 10 m and an aperture of 2–7 mm and so may be referred to as a mesofracture. Measurements indicate that U was transported along the 13.5-m N fracture, away from the Nopal I deposit, for a distance of at least 23.2 m; projecting the U concentration trend to local background values suggests the likelihood of anomalous U transport to about 26.3 m W of the edge of the deposit. The average U concentration along that length (based on a linear fit to the concentrations outside the deposit) is 720 ppm U. Therefore:

$$\text{U content} = (\text{length}) \times (\text{average aperture}) \times (\text{average U concentration}) = 91 \text{ ppm U m}^2 \quad (4\text{-}6)$$

This value represents the 2D U content of the portion of the 13.5-m N fracture outside the deposit. Regardless of the amount of U that may have been transported along this path, 91 ppm U m^2 is the amount that was retarded during mesofracture flow and retained to the present.

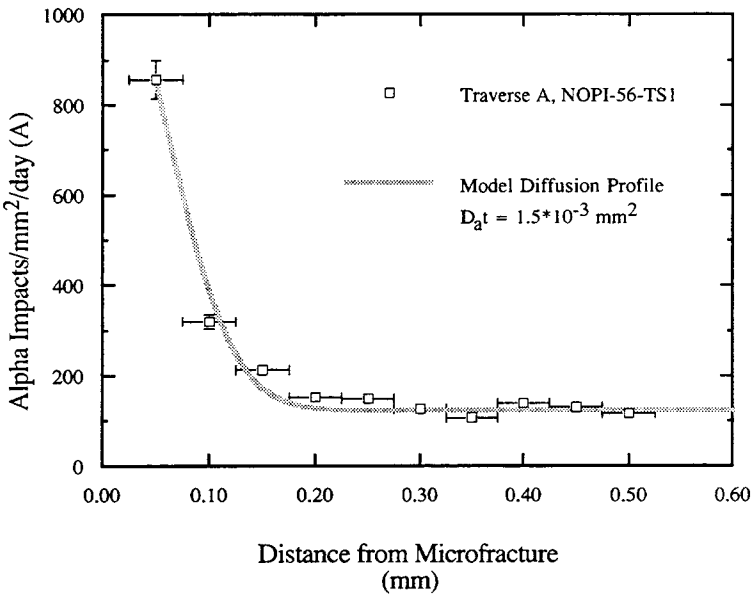

(a)

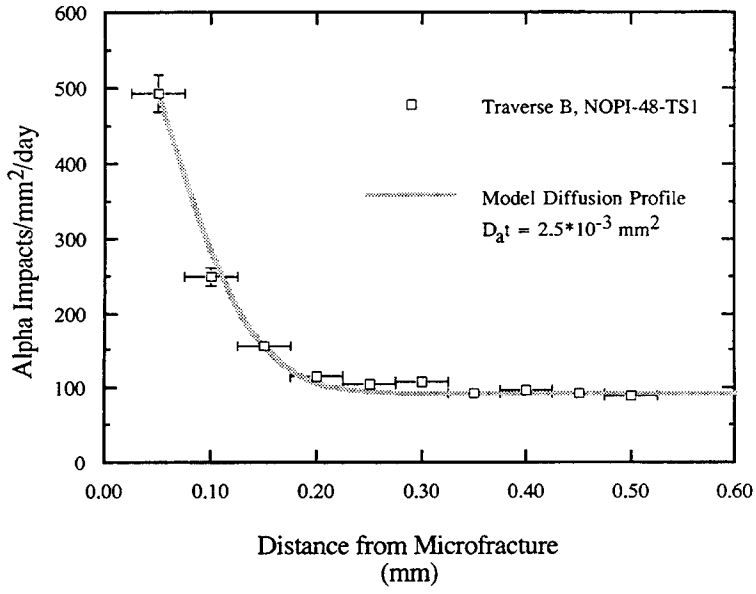

(b)

Figure 4-14. These plots show variations in alpha impact density adjacent to a microfracture. These data are interpreted as concentration profiles of U in the tuff matrix next to the microfracture. Error bars for distance are constant and correspond to the distance interval counted for each measurement. Alpha impact density errors are 1 sigma uncertainties. Stippled lines are profiles calculated as the best fit of the diffusion equation to the solid U concentrations using the measured alpha impact density for the first interval adjacent to the microfractures as a boundary condition for U°.

Similarly, the amount of U that was sequestered until present after transport out of the 13.5-m N fracture and into the microfracture network may be estimated by considering the portion of the system bounded to the E by the edge of the deposit, to the W by the projected limit of anomalous U concentration in the 13.5-m N fracture (26.3 m from the edge of the deposit), and bounded to the N and S by systematically variable distances corresponding to the limits of anomalous U concentration measured along the perpendicular traverses (Figure 4-11). Using these area limits, and linear interpolations of U concentration between adjacent traverses, the U content of the microfractured rock enclosing the 13.5-m N fracture is about 420 ppm U m^2.
Therefore, the dimensionless ratio:

$$\frac{(420 \text{ ppm U } m^2)}{(91 \text{ ppm U } m^2)} = 5 \qquad (4\text{-}7)$$

describes the amount of U retained during transport into the microfracture network adjacent to the 13.5-m N fracture compared to the amount of U retained during transport within the 13.5-m N fracture. Because (as detailed in Section 4.3) the lengths of the anomalous U paths into the microfracture network are minima, this ratio is also a minimum. Whatever the mechanisms for the U retardation (e.g., precipitation, sorption), it appears that much more U is retained within the microfracture network than within the mesofracture along which the U was transported to the microfracture network.

The relative effectiveness of matrix retardation of U at Nopal I may be estimated using measurements from the microfracture autoradiography presented in Section 4.5. These microfractures are largely filled with uranophane [$Ca(UO_2)_2Si_2O_7 \cdot 6H_2O$], which has a U concentration of 5.6×10^5 ppm. The microfractures studied have apertures varying from 100 to 230 μm. Using 100 μm, the 1D U content is 5.6×10^4 ppm U mm. Autoradiographic measurements show transport of U out from the uranophane-bearing microfractures to a maximum distance of 0.28 mm. Based on the specific activity of ^{238}U, assuming secular equilibrium (consistent with the location of the samples within the deposit and U-series measurements on other samples from within the deposit, Section 3.6), and an alpha particle attenuation in tuff matrix of 4 μm, the average transported U content along these matrix paths is about 9,000 ppm U.

The 1D U content along the matrix diffusion path is:

$$(9{,}000 \text{ ppm U}) \times (0.28 \text{ mm}) = 2{,}520 \text{ ppm U mm} \qquad (4\text{-}8)$$

and the ratio of the matrix U content to the microfracture U content is:

$$\frac{(2{,}520 \text{ ppm U mm})}{(5.6 \times 10^4 \text{ ppm U mm})} = 0.05 \qquad (4\text{-}9)$$

This analysis suggests that the amount of U retarded in the matrix (e.g., by sorption or other mechanisms) surrounding the microfractures is only 5 percent of the U retarded within the microfracture (e.g., by precipitation as uranophane). Further, 5 percent is a maximum value for U retardation within the matrix because this estimate is based on the maximum matrix path length (0.28 mm) and a minimum fracture aperture (100 μm).

5 CONCLUSIONS

Data presented here document the distributions of U within and around the Nopal I deposit and the transport of U away from the deposit mainly along fracture paths. U-series isotopic measurements indicate mobilization of U from the deposit within the last 1 Ma. This observation is consistent with U-series dating of samples within and outside of the deposit showing significant U transport at about 54 Ka. Both the general U distribution within the deposit and the U concentrations within an individual major fracture appear to be related to secondary non-U mineral occurrence. These relationships suggest remobilization of U by oxidizing, low-pH fluids and transport away from the deposit. U-bearing fluids moving away from the deposit appear to have deposited U as the fluid interacted physically and/or chemically with the wall rocks of the fracture paths.

Greater transport distances were achieved along a few relatively continuous mesofractures (e.g., fractures with apertures > 1 mm and traces extending more than 10 m) than through the general fracture network composed of thousands of less continuous microfractures (e.g., fractures with apertures $<< 1$ mm and traces on the order of cm) within and surrounding the deposit. U transport away from the deposit appears to be largely independent of the general fracture network pattern; this interpretation is supported by fractal analyses of the patterns suggesting that this result is insensitive to the scale at which the observations were made. Transport of U away from the Nopal I deposit along effective horizontal mesofracture paths achieved maximum distances at least 20 times greater than transport of U through tuff with a complex network of microfractures. Transport of U away from individual microfractures into homogeneous, unfractured (at optical microscopy scales) tuff matrix appears limited to distances less than 1 mm.

Inventories of U retarded and retained (e.g., by sorption, precipitation, co-precipitation) along different types of transport paths vary greatly. U distribution patterns along and around a mesofracture at Nopal I indicate U transport along a two-stage path: (i) transport along the mesofracture, then (ii) transport out of the mesofracture into a complex network of microfractures (linear fracture densities > 1 fracture/cm) through which the mesofracture passes. The amount of U retained within the mesofracture is 5 times less than the amount of U retained within the microfracture network of the tuff surrounding the mesofracture. Data from individual microfractures with high U concentrations (e.g., 5.6×10^5 ppm) indicate that the amount of U transported out of the microfracture into the tuff matrix adjacent to the microfracture is only 5 percent of the U retarded within the microfracture (mainly by precipitation as uranophane). This analysis suggests a relative ranking for U retention: (i) microfracture network retention $>>$ mesofracture retention, and (ii) individual microfracture retention $>>$ matrix retention.

6 REFERENCES

Alba, L.A. , and R. Chavez. 1974. K-Ar ages of volcanic rocks from the central Sierra Peña Blanca, Chihuahua, Mexico. *Isochron West* 10: 21–23.

Basham, I.R. 1981. Some applications of autoradiographs in textural analysis of U bearing samples—discussion. *Economic Geology* 76: 974–977.

Calas, G. 1977. Les Phenomenes d'Alteration Hydrothermale et leur Relation avec les Mineralisations Uraniferes en Milieu Volcnique: Le cas des Ignimbrites Tertiaires de la Sierra de Peña Blanca, Chihuahua (Mexique). *Sciences Geologiques Bulletin* 30: 3–18.

Cardenas-Flores, D. 1985. Volcanic stratigraphy and U-Mo mineralization of the Sierra de Peña Blanca District, Chihuahua, Mexico. U Deposits in Volcanic Rocks. *Proceedings of a Technical Committee Meeting, El Paso, TX.* Austria: International Atomic Energy Agency. IAEA-TC-490: 125–136.

Dickson, B.L., and A.L. Herczeg. 1992. Deposition of trace elements and radionuclides in the spring zone, Lake Tyrrell, Victoria, Australia. *Chemical Geology* 96: 151–166.

George-Aniel, B., J.L. Leroy, and B. Poty. 1991. Volcanogenic U mineralization in the Sierra Peña Blanca District, Chihuahua, Mexico: Three genetic models. *Economic Geology* 86: 233–248.

George-Aniel, B.G., J. Leroy, and B. Poty. 1985. U deposits of the Sierra Peña Blanca. U Deposits in Volcanic Rocks. *Proceedings of a Technical Committee Meeting, El Paso, TX.* Austria: International Atomic Energy Agency. IAEA-TC-490: 175–186.

Ghosh, A., and J.J.K. Daemen. 1993. Fractal characteristics of rock discontinuities. *Engineering Geology* 34: 1–9.

Goodell, P.C. 1981. Geology of the Peña Blanca U deposits, Chihuahua, Mexico. *U in Volcanic and Volcaniclastic Rocks—AAPG Studies in Geology No. 13.* P.C. Goodell and A.C. Waters, eds. El Paso, TX: American Association of Petroleum Geologists: 275–291.

Guthrie, V. 1991. Determination of recent ^{238}U, ^{234}U and ^{230}Th mobility in granitic rocks: Application of a natural analogue to the high-level waste repository environment. *Applied Geochemistry* 6: 63–74.

Ildefonse, P., P. Agrinier, and J.-P. Muller. 1990a. Crystal chemistry and isotope geochemistry of alteration associated with the U Nopal 1 deposit, Chihuahua, Mexico. *Geochemistry of the Earth's Surface and of Mineral Formation.* Aix en Provence, France: 371–372.

Ildefonse, P., J.-P. Muller, and G. Calas. 1990b. Assessment of radionuclide migration in natural analogues by radiation-induced centers in kaolinites. *Symposium Proceedings of the Scientific Basis for Nuclear Waste Management XIV.* T.A. Abrajano Jr. and L.H. Johnson, eds. Boston, MA: Materials Research Society 212: 474.

Ildefonse, P., J.-P. Muller, B. Clozel, and G. Calas. 1990c. Study of two alteration systems as natural analogues for radionuclide release and migration. *Engineering Geology* 29: 413–439.

Leroy, J.L., B. Aniel, and B. Poty. 1987. The Sierra Peña Blanca (Mexico) and the Meseta Los Frailes (Bolivia); The U concentration mechanisms in volcanic environment during hydrothermal processes. *International Colloquium on Concentration Mechanisms of U in geological environments–1985.* B. Poty and M. Pagel, eds. Nancy, France: 211–234.

Leslie, B.W, E.C. Pearcy, W.M. Murphy, and J.D. Prikryl. 1993a. Fracture and Matrix Controlled U Migration at the Peña Blanca Natural Analog Site. *Fourth International Conference on the Chemistry and Migration Behavior of the Actinides and Fission Products in the Geosphere.* Charleston, SC: 110.

Leslie, B.W, E.C. Pearcy, and J.D. Prikryl. 1993b. Geochemical Natural Analogs. *NRC High-Level Radioactive Waste Research at CNWRA January—June 1992.* W.C. Patrick, ed. NUREG/CR-5817. Washington, DC: Nuclear Regulatory Commission: 3(1).

Leslie, B.W, E.C. Pearcy, and J.D. Prikryl. 1993c. Oxidative alteration of uraninite under hydrologically unsaturated conditions at Peña Blanca, Chihuahua, Mexico: contaminant transport and source term constraints for the proposed repository at Yucca Mountain, Nevada. *Symposium Proceedings of the 294 Scientific Basis for Nuclear Waste Management XVI.* C.G. Interrante and R.T. Pabalan, eds. Pittsburgh, PA: Materials Research Society 294: 505–512.

Mandelbrot, B.B. 1982. *The Fractal Geometry of Nature.* San Francisco, CA: Freeman.

Muller, J.-P., P. Ildefonse, and G. Calas. 1990. Paramagnetic defect centers in hydrothermal kaolinite from an altered tuff in the Nopal U deposit, Chihuahua, Mexico. *Clays and Clay Mineralogy* 38: 600–608.

Murphy, W.M. and E.C. Pearcy. 1992. Source-term constraints for the proposed repository at Yucca Mountain, Nevada, derived from the natural analog at Peña Blanca, Mexico. *Symposium Proceedings of the Scientific Basis for Nuclear Waste Management XV.* C.G. Sombret, ed. Pittsburgh, PA: Materials Research Society 257: 521–527.

Murphy, W.M., E.C. Pearcy, and P.C. Goodell. 1991. Possible analog research sites for the proposed high-level nuclear waste repository in hydrologically unsaturated tuff at Yucca Mountain, Nevada. *Fourth Natural Analogue Working Group Meeting and Poços de Caldas project final workshop.* B. Come and N.A. Chapman, eds. Brussels: Commission of the European Communities: Final Report n° EUR 13014 EN: 267–276.

Neretnieks, I. 1980. Diffusion in the rock matrix: An important factor in radionuclide retardation? *Journal of Geophysical Research* 85: 4,379–4,397.

Nordstrom, D.K. 1982. *Aqueous pyrite oxidation and the consequent formation of secondary iron minerals.* Acid Sulfate Weathering. Soil Science Society of America. Special Publication Number 10: 37–56.

Pearcy, E.C., and W.M. Murphy. 1991. *Geochemical Natural Analogs Literature Review*. CNWRA 90-008. San Antonio, TX: Center for Nuclear Waste Regulatory Analyses.

Pearcy, E.C., and W.M. Murphy. 1992. *Site Selection and Workplan Report for the Geochemical Natural Analog Research Project*. CNWRA 92-014. San Antonio, TX: Center for Nuclear Waste Regulatory Analyses.

Pearcy, E.C., W.M. Murphy, R.T. Green, B.W. Leslie, and J.D. Prikryl. 1993a. Geochemical natural analogs. *NRC High-Level Radioactive Waste Research at CNWRA Calendar Year 1991*. W.C. Patrick, ed. NUREG/CR-5817. Washington, DC: Nuclear Regulatory Commission: 7-1 to 7-32.

Pearcy, E.C., J.D. Prikryl, W.M. Murphy, and B.W. Leslie. 1993b. *U mineralogy of the Nopal I Natural Analog Site, Chihuahua, Mexico*. CNWRA 93-012. San Antonio, TX: Center for Nuclear Waste Regulatory Analyses.

Turner, D.R. 1991. *Sorption Modeling for High-Level Waste Performance Assessment: A Literature Review*. CNWRA 91-011. San Antonio, TX: Center for Nuclear Waste Regulatory Analyses.

U.S. Department of Commerce. 1965. *World Weather Records 1951-60, Vol. 1 North America*. Washington, DC: U.S. Department of Commerce.

U.S. Environmental Protection Agency. 1989. *Environmental Radiation Protection Standards for Management and Disposal of Spent Nuclear Fuel, High-Level and Transuranic Radioactive Wastes*. Title 40, Protection of the Environment, Part 191 (40 CFR 191.13). Washington, DC: U.S. Government Printing Office.

Voss, R.F. 1988. The science of fractal images. *Fractals in Nature*. H.-O. Peitgen and D. Saupe, eds. New York, NY: Springer: 1-70.

Wescott, R.G., M.P. Lee, N.A. Eisenberg, and T.J. McCartin, eds. 1994. *Phase 2 Demonstration of the NRC's Capability to Conduct a Performance Assessment for a High-Level Waste Repository*. NUREG-1464. Washington, DC: U.S. Nuclear Regulatory Commission. In preparation.